

Azimuthal seismic dispersion analysis and inversion based on a frequency-dependent fractured model

Jing Ba¹, Guangtan Huang², José M. Carcione³, and Davide Gei³

ABSTRACT

Wave velocity dispersion and attenuation due to wave-induced fluid flow are important properties for seismic exploration studies of fracture characterization and hydrocarbon identification. Existing seismic inversions are based primarily on an isotropic theory. However, dispersion and anisotropy should also be considered together. Based on a fracture model describing attenuation, we introduce a frequency-dependent stiffness matrix for azimuthal dispersion analysis, where the dispersion gradient of fracture weakness is a novel fluid indicator. Then, a method of inverting the frequency-dependent amplitude changes with angle and azimuth is developed to extract the fluid indicator from the seismic data. An inversion test on field data demonstrates the validity of our method.

INTRODUCTION

Seismic data are associated with a large amount of information regarding the tectonics and lithology of the subsurface. When seismic waves travel through fractured reservoirs, the recorded data may contain information about rock anisotropy (Crampin, 1984; Hsu and Schoenberg, 1993; Bakulin et al., 2000a, 2000b; Carcione and Picotti, 2012; Carcione et al., 2012; Oh and Alkhalifah, 2016). A single set of aligned vertical fractures embedded in an isotropic host rock can be regarded as an effective transversely isotropic medium with a horizontal axis of symmetry (HTI). As demonstrated by numerical simulations, laboratory experiments, and seismic inversions, fracture-induced anisotropy causes amplitude variation with azimuth (AVAZ) (Henneke, 1972; Keith and Crampin, 1977; Rüger, 1998; Chen et al., 2015, 2017, 2018; Pan et al., 2018; Zhang et al., 2021, 2022). Fractures are channels of accumulation and migration

of fluids; therefore, the characterization of the fractures and the identification of saturating fluids will contribute to the exploration and development of fractured reservoirs.

The type of saturating fluids can be estimated from seismic data considering specific fluid indicators. A variety of indicators have been proposed, such as combinations of elastic and reservoir properties and frequency-dependent inversions (Carcione, 2000, 2022; Gurevich, 2003; Chapman et al., 2006; Zhao et al., 2017; Guo et al., 2018a, 2018b). The combination of P- and S-wave velocity ratio, Poisson's ratio, and Lamé constants exploits the assumption that S-wave velocity is affected only by the rock skeleton, whereas P-wave velocity changes are correlated to type fluid (Goodway, 2001; Zimmer, 2003; Zhao et al., 2014). In anisotropic media, the ratio of normal to shear fracture weakness is a fluid indicator (Schoenberg and Sayers, 1995; Pan et al., 2017). Peng et al. (2013) adopt the anisotropic gradient to identify fluid content. Russell et al. (2003, 2011) propose a decoupled fluid indication factor based on the Gassmann equation. Huang et al. (2021a) propose an improved method for the decoupling of elastic parameters based on the Hertz-Mindlin model and presented a direct inversion of fluid properties for sandstones. These methods depend on specific rock-physics models that must be calibrated to the lithotype of the reservoir considered in the inversion.

Frequency-dependent seismic anomalies due to the saturating fluid are described by the wave-induced fluid flow (WIFF) effect, an attenuation mechanism that implies velocity dispersion (velocity dependence on frequency, not to be confused with loss of amplitude due to geometric spreading). The dispersion can be a fluid indicator and in the case of fractures, the fracture weaknesses are frequency dependent. A frequency-dependent amplitude-variation-with-offset (AVO) inversion is proposed by Castagna et al. (2003) as an effective approach to extract dispersion features. Wilson et al. (2009) and Wu et al. (2015) propose a frequency-dependent AVO inversion to extract the P-wave velocity dispersion gradient. Recently, different methods have been proposed but mainly based on the assumption of

Manuscript received by the Editor 6 June 2024; revised manuscript received 12 January 2025; published ahead of production 17 February 2025; published online 23 April 2025.

¹Hohai University, School of Earth Sciences and Engineering, Nanjing, China. E-mail: jba@hhu.edu.cn.

²Chinese Academy of Sciences, State Key Laboratory of Geomechanics and Geotechnical Engineering Safety, Institute of Rock and Soil Mechanics, Wuhan, China. E-mail: gthuang@whrsm.ac.cn (corresponding author).

³National Institute of Oceanography and Applied Geophysics — OGS, Trieste, Italy. E-mail: jose.carcione@gmail.com; dgei@inogs.it.

© 2025 Society of Exploration Geophysicists. All rights reserved.

isotropic media (e.g. Huang et al., 2017, 2021b; Luo et al., 2018). In addition to the WIFF mechanism, scattering also induces frequency-dependent variations of the elastic properties (Kumar et al., 2019). In this work, we assume a homogeneous medium and neglect scattering effects.

Seismic propagation induces local fluid flow between the soft microfractures and the host porous skeleton. WIFF effects lead to velocity dispersion, attenuation, and frequency-dependent anisotropy. Numerous models, incorporating microfractures and intergranular pores in the host rock or considering these fractures as host perturbations, have explained WIFF effects in anisotropic media (Hudson et al., 1996; Chapman et al., 2002; Chapman, 2003; Jakobsen et al., 2003; Brajanovski et al., 2005; Galvin and Gurevich, 2009; Gurevich et al., 2009; Ba et al., 2017; Fu et al., 2018, 2020).

Although the previous studies have been performed on nonlinear fractured rock-physics models to derive the frequency-dependent stiffness matrices for AVAZ analysis (Guo et al., 2020; Liu et al., 2021), they do not explicitly quantify the relationships between frequency-dependent variables and fracture fluid properties. In addition, the latest inversion approaches basically assume the Thomsen anisotropy parameters to be frequency dependent without directly relating them to fracture properties (Li et al., 2024). In this work, a modified Hudson model (Pointer et al., 2000) combined with the Schoenberg model is introduced, where fracture parameters are expressed as frequency-dependent functions. This allows us to establish the normal fracture weakness parameter as a function directly related to fracture fluid. Furthermore, we apply a Taylor expansion to this function, providing a more physically consistent method than simply assuming frequency-dependent anisotropic parameters. Then, a frequency-dependent AVAZ inversion is performed to extract the dispersion of fracture weaknesses. Finally,

we demonstrate the performance of the proposed inversion method on field data examples.

METHODOLOGY

Stiffness matrix of rocks with interconnected aligned fractures

Table 1 provides the list of symbols. According to Hudson (1981), the general form of the stiffness matrix \mathbf{C} of rocks with aligned fractures, accurate to the first order, is

$$\mathbf{C} = \mathbf{C}^0 + \mathbf{C}^1, \quad (1)$$

where \mathbf{C}^0 is the stiffness matrix of the host matrix, and \mathbf{C}^1 is the first-order correction for the effect of the embedded fractures. Let the x_3 -axis be perpendicular to the layering, and x_1 and x_2 are mutually orthogonal axes parallel to the stratum. By assuming that the normal to the fractures is aligned along a preferred spatial axis, x_1 , the associated stiffness matrix is

$$\mathbf{C} = \begin{bmatrix} M_b \left(1 - \frac{M_b}{\mu_b} e U_{33}\right) \lambda_b \left(1 - \frac{M_b}{\mu_b} e U_{33}\right) \lambda_b \left(1 - \frac{M_b}{\mu_b} e U_{33}\right) & 0 & 0 & 0 & 0 & 0 \\ \lambda_b \left(1 - \frac{M_b}{\mu_b} e U_{33}\right) & M_b \frac{\lambda_b^2}{\mu_b} e U_{33} & \lambda_b \left(1 - \frac{\lambda_b}{\mu_b} e U_{33}\right) & 0 & 0 & 0 \\ \lambda_b \left(1 - \frac{M_b}{\mu_b} e U_{33}\right) & \lambda_b \left(1 - \frac{\lambda_b}{\mu_b} e U_{33}\right) & M_b \frac{\lambda_b^2}{\mu_b} e U_{33} & 0 & 0 & 0 \\ 0 & 0 & 0 & \mu_b & 0 & 0 \\ 0 & 0 & 0 & 0 & \mu_b (1 - e U_{11}) & 0 \\ 0 & 0 & 0 & 0 & 0 & \mu_b (1 - e U_{11}) \end{bmatrix}, \quad (2)$$

where M_b and μ_b are the P- and S-wave moduli of the host matrix, respectively, and λ_b is the first Lamé constant. The medium of the host matrix can be assumed isotropic or transverse isotropy media with a vertical axis of symmetry (VTI). The isotropic host matrix becomes an HTI medium when adding vertical fractures, whereas a VTI host becomes an orthorhombic medium. Equation 2 corresponds to the first case. Moreover, e is the fracture density, and U_{11} and U_{33} are fracture parameters related to the host medium and saturating material, respectively.

Here, to fully incorporate the WIFF effect of fluids within fractures, an improved Hudson model (Pointer et al., 2000) coupled with the Schoenberg model is introduced. It yields the stiffness matrix expression for a fluid-saturated state, and the detailed derivation can be found in Appendix A. The stiffness matrix is decomposed into three components: the host matrix \mathbf{C}_b , the crack component $\mathbf{C}_{\text{crack}}$, and the fluid-related part $\mathbf{C}_{\text{fluid}}$, as follows:

$$\mathbf{C} = \mathbf{C}_b + \mathbf{C}_{\text{crack}} + \mathbf{C}_{\text{fluid}}, \quad (3)$$

where

$$\mathbf{C}_b = \begin{bmatrix} M_b & \lambda_b & \lambda_b & 0 & 0 & 0 \\ \lambda_b & M_b & \lambda_b & 0 & 0 & 0 \\ \lambda_b & \lambda_b & M_b & 0 & 0 & 0 \\ 0 & 0 & 0 & \mu_b & 0 & 0 \\ 0 & 0 & 0 & 0 & \mu_b & 0 \\ 0 & 0 & 0 & 0 & 0 & \mu_b \end{bmatrix}, \quad (4)$$

Table 1. List of symbols.

Symbol	Description	Symbol	Description
λ, μ	Lamé parameters	\mathbf{C}	Stiffness matrix
\mathbf{C}^0	Stiffness matrix of host	\mathbf{C}^1	First-order correction of \mathbf{C}
K	Bulk modulus	M	P-wave modulus
E	Young's modulus	ν	Poisson's ratio
c_{IJ}	Stiffness	ρ	Density
$c_{b,IJ}$	Stiffness of host matrix	ρ_b	Density of host matrix
M_b	P-wave modulus of host matrix	λ_b, μ_b	Lamé parameters of host matrix
R_{PP}	P-P wave reflection coefficient	R_{PP}^{iso}	Isotropic part of R_{PP}
R_{PP}^{ani}	Anisotropic part of R_{PP}	q	Volume proportion of fluid
θ	Incidence angle	ϕ	Azimuthal angle
e	Fracture density	χ	Aspect ratio of fracture
Δ	Perturbation	δ_N, δ_T	Fracture weaknesses
δ_N, δ_T	Fracture weaknesses	$\delta_N^{\text{dry}}, \delta_T^{\text{dry}}$	Dry fracture weaknesses
η	Viscosity	\mathbf{W}	Wavelet matrix
\mathbf{S}	Seismic data	\mathbf{S}^*	Azimuthal difference seismic data
g	μ_b/M_b	α	P-wave velocity
f	Frequency	f_{dom}	Dominant frequency

$$\mathbf{C}_{\text{crack}} = - \begin{bmatrix} \frac{M_b \delta_N^{\text{dry}}}{g} & \frac{\lambda_b \delta_N^{\text{dry}}}{g} & \frac{\lambda_b \delta_N^{\text{dry}}}{g} & 0 & 0 & 0 \\ \frac{\lambda_b \delta_N^{\text{dry}}}{g} & \frac{\lambda_b^2 \delta_N^{\text{dry}}}{\mu} & \frac{\lambda_b \delta_N^{\text{dry}}}{g} & 0 & 0 & 0 \\ \frac{\lambda_b \delta_N^{\text{dry}}}{g} & \frac{\lambda_b \delta_N^{\text{dry}}}{g} & \frac{\lambda_b^2 \delta_N^{\text{dry}}}{\mu} & 0 & 0 & 0 \\ 0 & 0 & 0 & 0 & \delta_T^{\text{dry}} & 0 \\ 0 & 0 & 0 & 0 & 0 & \delta_T^{\text{dry}} \end{bmatrix}, \quad (5)$$

and

$$\mathbf{C}_{\text{fluid}} = (\omega^2 \Gamma^2 + i\omega \Gamma) \begin{bmatrix} \frac{M_b \delta_N^{\text{dry}}}{g} & \frac{\lambda_b \delta_N^{\text{dry}}}{g} & \frac{\lambda_b \delta_N^{\text{dry}}}{g} & 0 & 0 & 0 \\ \frac{\lambda_b \delta_N^{\text{dry}}}{g} & \frac{\lambda_b^2 \delta_N^{\text{dry}}}{\mu} & \frac{\lambda_b \delta_N^{\text{dry}}}{g} & 0 & 0 & 0 \\ \frac{\lambda_b \delta_N^{\text{dry}}}{g} & \frac{\lambda_b \delta_N^{\text{dry}}}{g} & \frac{\lambda_b^2 \delta_N^{\text{dry}}}{\mu} & 0 & 0 & 0 \\ 0 & 0 & 0 & 0 & 0 & 0 \\ 0 & 0 & 0 & 0 & 0 & 0 \\ 0 & 0 & 0 & 0 & 0 & 0 \end{bmatrix}, \quad (6)$$

where ω denotes $g = \mu_b/M_b$, and δ_N^{dry} and δ_T^{dry} are the normal and tangential weaknesses of the dry fractures, respectively. Here, Γ represents the relaxation time, which is a function of water saturation. The detailed expression can be found in Appendix A.

In this work, we consider fracture weakness as a frequency-dependent parameter, while a partial decoupling of the fracture weakness is performed. An idealized full decoupling is still not achieved. In the inversion process, we focus on the dispersion of fracture weakness, and the inversion based on the fluid factor is not conducted. In a future study, a method of better/full decoupling of the fracture weakness could be proposed to isolate the parameters that are exclusively related to fluid, based on which the seismic inversion could be improved with the accuracy and applicability.

The stiffness matrix of rocks with partially saturated fractures is frequency dependent, and the ratio of the imaginary and real parts of matrix varies with frequency, fluid saturation, fracture aspect ratio, and fracture density.

In the presence of weak anisotropy, the stiffness components c_{ijkl} at a weak-contrast interface can be considered to be perturbed on the basis of a reference (or background) medium. Thus, the real and imaginary parts of the perturbation are, respectively,

$$R[\Delta \mathbf{C}(\omega)] = - \begin{bmatrix} (1-\omega^2 \Gamma^2) \frac{M_b \delta_N^{\text{dry}}}{g} & (1-\omega^2 \Gamma^2) \frac{\lambda_b \delta_N^{\text{dry}}}{g} & (1-\omega^2 \Gamma^2) \frac{\lambda_b \delta_N^{\text{dry}}}{g} & 0 & 0 & 0 \\ (1-\omega^2 \Gamma^2) \frac{\lambda_b \delta_N^{\text{dry}}}{g} & (1-\omega^2 \Gamma^2) \frac{\lambda_b^2 \delta_N^{\text{dry}}}{\mu} & (1-\omega^2 \Gamma^2) \frac{\lambda_b \delta_N^{\text{dry}}}{g} & 0 & 0 & 0 \\ (1-\omega^2 \Gamma^2) \frac{\lambda_b \delta_N^{\text{dry}}}{g} & (1-\omega^2 \Gamma^2) \frac{\lambda_b \delta_N^{\text{dry}}}{g} & (1-\omega^2 \Gamma^2) \frac{\lambda_b^2 \delta_N^{\text{dry}}}{\mu} & 0 & 0 & 0 \\ 0 & 0 & 0 & 0 & 0 & 0 \\ 0 & 0 & 0 & 0 & \delta_T^{\text{dry}} & 0 \\ 0 & 0 & 0 & 0 & 0 & \delta_T^{\text{dry}} \end{bmatrix},$$

$$I[\Delta \mathbf{C}(\omega)] = \omega \Gamma \begin{bmatrix} \frac{M_b \delta_N^{\text{dry}}}{g} & \frac{\lambda_b \delta_N^{\text{dry}}}{g} & \frac{\lambda_b \delta_N^{\text{dry}}}{g} & 0 & 0 & 0 \\ \frac{\lambda_b \delta_N^{\text{dry}}}{g} & \frac{\lambda_b^2 \delta_N^{\text{dry}}}{\mu} & \frac{\lambda_b \delta_N^{\text{dry}}}{g} & 0 & 0 & 0 \\ \frac{\lambda_b \delta_N^{\text{dry}}}{g} & \frac{\lambda_b \delta_N^{\text{dry}}}{g} & \frac{\lambda_b^2 \delta_N^{\text{dry}}}{\mu} & 0 & 0 & 0 \\ 0 & 0 & 0 & 0 & 0 & 0 \\ 0 & 0 & 0 & 0 & 0 & 0 \\ 0 & 0 & 0 & 0 & 0 & 0 \end{bmatrix}. \quad (7)$$

The azimuthal dependence of the perturbation is induced by the dry fractures, while the frequency-dependent perturbation is associated with fracture fillings. We consider a two-layer model to compare the real and imaginary parts of the frequency-dependent parameters, where the material properties are reported in Table 2. The model is composed of isotropic media overlying a fractured reservoir (with HTI symmetry, horizontal transverse isotropy). Figure 1a and 1b shows the real (upper panel) and imaginary (lower panel) parts of U_{33} and U_{11} with the properties of the lower layer (equation A-3). The imaginary part of U_{33} is much smaller than the real part at the seismic frequency range, and U_{11} is not a parameter that varies with frequency. Thus, for the U_{33} and U_{11} parameters, it is the real part that mainly affects them, while the imaginary part has very little effect on them. In addition, if we consider the imaginary part (see next section) it is also difficult to apply the approximate reflection coefficients. Then, the seismic wavefield simulation verifies that the effect of the imaginary part can be neglected.

To observe the effect of the imaginary part of the stiffness on the seismic data, we adopt a generalized propagation matrix (GPM) (Carcione, 2022) as forward operator to simulate angle gathers. We introduce the complex stiffness and its real part to the GPM method and obtain the corresponding gathers. Figure 2a and 2b corresponds to the angle gathers for zero azimuth by using the GPM with the complex and real part of the stiffness matrix, respectively, and Figure 2c shows the difference between the simulated gathers. The angle gather simulated by neglecting the imaginary part agrees relatively well with the exact one. Indeed, the imaginary part usually affects the variation of the phase but when the imaginary part is much smaller than the real part, such an influence is negligible.

Table 2. Material properties of two-layer model.

	Property	Value
Upper layer	P-wave modulus M_b	20.4 GPa
	Shear modulus μ_b	4.04 GPa
	Bulk density ρ^b	2.43 g/cm ³
	Fracture density e	0
	Aspect ratio χ	0
	Volume proportion of gas q_g	0.98
Lower layer	P-wave modulus M_b	23.3 GPa
	Shear modulus μ_b	6.31 GPa
	Bulk density ρ^b	2.28 g/cm ³
	Fracture density e	0.01
	Aspect ratio χ	0.001
	Volume proportion of gas q_g	0.7
Fluid	Brine P-wave velocity α_{brine}	1.47 km/s
	Brine bulk density ρ_{brine}	1.04 g/cm ³
	Brine viscosity η_w	1×10^{-3} Pa · s
	Oil P-wave velocity α_{oil}	0.750 km/s
	Oil bulk density ρ_{oil}	0.70 g/cm ³
	Oil viscosity η_o	20×10^{-3} Pa · s
	Gas P-wave velocity α_{gas}	0.603 km/s
Gas bulk density ρ_{gas}	0.0011 g/cm ³	
	Gas viscosity η_g	1.8×10^{-5} Pa · s

Hence, we neglect the imaginary part of the stiffness matrix in the following analyses.

According to the Schoenberg model (Schoenberg and Protazio, 1992), the stiffness matrix is related to the isotropic host medium and the anisotropic perturbation as follows:

$$\mathbf{C} = \mathbf{C}_b + \Delta\mathbf{C} = \begin{bmatrix} M_b & \lambda_b & \lambda_b & 0 & 0 & 0 \\ \lambda_b & M_b & \lambda_b & 0 & 0 & 0 \\ \lambda_b & \lambda_b & M_b & 0 & 0 & 0 \\ 0 & 0 & 0 & \mu_b & 0 & 0 \\ 0 & 0 & 0 & 0 & \mu_b & 0 \\ 0 & 0 & 0 & 0 & 0 & \mu_b \end{bmatrix} - \begin{bmatrix} M_b\delta_N & \lambda_b\delta_N & \lambda_b\delta_N & 0 & 0 & 0 \\ \lambda_b\delta_N & \frac{\lambda_b^2}{M_b}\delta_N & \frac{\lambda_b^2}{M_b}\delta_N & 0 & 0 & 0 \\ \lambda_b\delta_N & \frac{\lambda_b^2}{M_b}\delta_N & \frac{\lambda_b^2}{M_b}\delta_N & 0 & 0 & 0 \\ 0 & 0 & 0 & 0 & 0 & 0 \\ 0 & 0 & 0 & 0 & \mu_b\delta_T & 0 \\ 0 & 0 & 0 & 0 & 0 & \mu_b\delta_T \end{bmatrix}. \quad (8)$$

By comparing equations 3 and 8, the fracture weaknesses are

$$\delta_N = \frac{4e}{3g(1-g)}(1 - \omega^2\Gamma^2), \quad \delta_T = \frac{16e}{3(3-2g)}, \quad (9)$$

where δ_N is a frequency-dependent parameter, and the related dispersion can be considered as an indicator for the fracture filling fluid.

FREQUENCY-DEPENDENT AVAZ INVERSION

The P-P wave approximate reflection coefficients (Chen et al., 2015; Pan et al., 2017) are

$$R_{PP}(\theta, \phi) = a_{M_b}(\theta)r_{M_b} + a_{\mu_b}(\theta)r_{\mu_b} + a_\rho(\theta)r_\rho + a_{\delta_N}(\theta, \phi)r_{\delta_N} + a_{\delta_T}(\theta, \phi)r_{\delta_T}, \quad (10)$$

where ϕ and θ are the azimuth and incidence angles, and

$$r_{M_b} = \frac{\Delta M_b}{M_b}, \quad r_{\mu_b} = \frac{\Delta \mu_b}{\mu_b}, \quad r_\rho = \frac{\Delta \rho}{\bar{\rho}}, \quad (11)$$

$$r_{\delta_N} = \Delta \delta_N, \quad r_{\delta_T} = \Delta \delta_T,$$

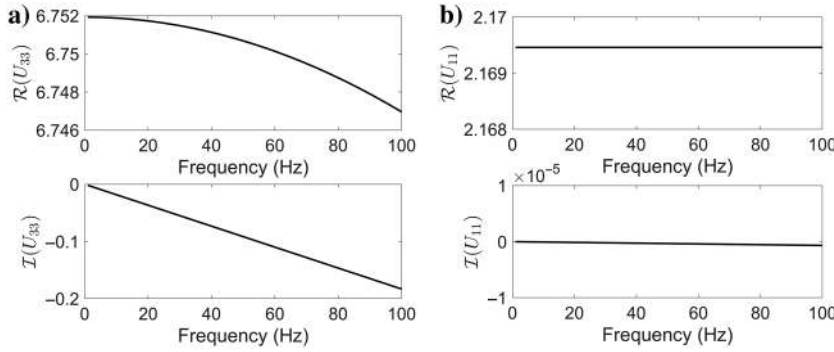


Figure 1. Real (top) and imaginary (bottom) parts of (a) U_{33} and (b) U_{11} for gas-bearing fractured rocks as a function of frequency.

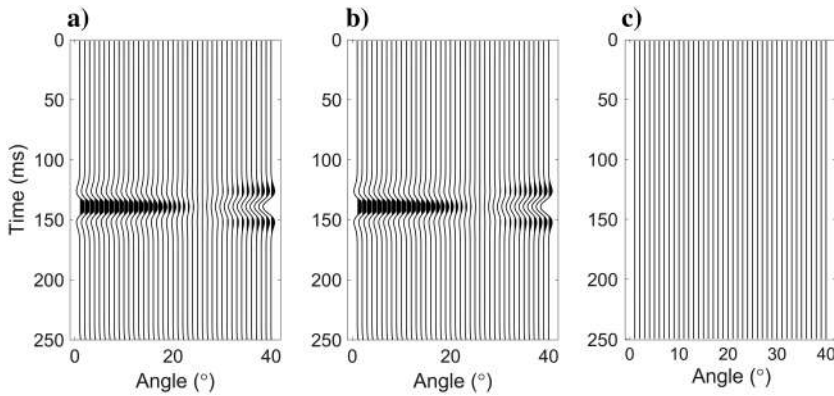


Figure 2. Simulated zero-azimuth angle gather of a two-layer model (Table 2) by using the GPM method with (a) the complex and (b) real part of the stiffness matrix, and (c) the difference.

where Δ and $\{\cdot\}$ denote the difference and average of the parameters between the upper and lower layers, and

$$a_{M_b} = \frac{1}{4\cos^2\theta}, \quad a_{\mu_b} = -2g\sin^2\theta, \quad (12)$$

$$a_\rho = \frac{1}{2} - \frac{1}{4\cos^2\theta},$$

$$a_{\delta_N} = \frac{1}{4\cos^2\theta} [2g(\sin^2\theta\sin^2\phi + \cos^2\theta) - 1]^2,$$

$$a_{\delta_T} = g\sin^2\theta\cos^2\phi(1 - \tan^2\theta\sin^2\phi).$$

As shown in equation 10, the reflection coefficient can be partitioned into two parts, i.e., an azimuth-dependent (anisotropic part) $R_{PP}^{\text{ani}}(\theta, \phi)$ and an azimuth-independent (isotropic part) $R_{PP}^{\text{iso}}(\theta)$.

Azimuthal seismic data can be considered as the reflectivity profile convolved with the seismic wavelet, such that

$$\mathbf{S}(\theta, \phi) = \mathbf{W}(\theta, \phi)\mathbf{R}_{PP}(\theta, \phi), \quad (13)$$

where \mathbf{W} and \mathbf{R}_{PP} are the wavelet matrix and P-P wave reflectivity. The wavelets with different incidence and azimuth angles are extracted from seismic data and well-log data, and then each frequency component is obtained using time-frequency analysis methods. The specific forms for \mathbf{S}_{PP} , \mathbf{R}_{PP} , and \mathbf{W} are

$$\mathbf{S}_{PP}(\theta, \phi) = \begin{bmatrix} s_{PP}(1, \theta, \phi) \\ s_{PP}(2, \theta, \phi) \\ \vdots \\ s_{PP}(i, \theta, \phi) \\ \vdots \\ s_{PP}(N, \theta, \phi) \end{bmatrix}, \quad \mathbf{R}_{PP}(\theta, \phi) = \begin{bmatrix} R_{PP}(1, \theta, \phi) \\ R_{PP}(2, \theta, \phi) \\ \vdots \\ R_{PP}(i, \theta, \phi) \\ \vdots \\ R_{PP}(N, \theta, \phi) \end{bmatrix},$$

$$\mathbf{W}(\theta, \phi) = \begin{bmatrix} w(1, \theta, \phi) & w(2, \theta, \phi) & \cdots & w(N, \theta, \phi) \\ w(2, \theta, \phi) & w(3, \theta, \phi) & \cdots & w(1, \theta, \phi) \\ \vdots & \vdots & \ddots & \vdots \\ w(i, \theta, \phi) & w(i+1, \theta, \phi) & \cdots & w(N-i+1, \theta, \phi) \\ \vdots & \vdots & \ddots & \vdots \\ w(N, \theta, \phi) & w(1, \theta, \phi) & \cdots & w(N-1, \theta, \phi) \end{bmatrix}, \quad (14)$$

where i refers to the temporal sample.

Thus, based on equation 19, the amplitude difference at different azimuths is

$$\begin{aligned} \mathbf{S}^*(\theta, \Delta\phi_{ij}) &= \mathbf{S}(\theta, \phi_i) - \mathbf{S}(\theta, \phi_j) \\ &= \overline{\mathbf{W}}(\theta, \phi_i, \phi_j) [\mathbf{R}_{PP}(\theta, \phi_i) - \mathbf{R}_{PP}(\theta, \phi_j)] \\ &= \overline{\mathbf{W}}(\theta, \phi_i, \phi_j) [\mathbf{R}_{PP}^{\text{iso}}(\theta) + \mathbf{R}_{PP}^{\text{ani}}(\theta, \phi_i) - \mathbf{R}_{PP}^{\text{iso}}(\theta) \\ &\quad - \mathbf{R}_{PP}^{\text{ani}}(\theta, \phi_j)] \\ &= \overline{\mathbf{W}}(\theta, \phi_i, \phi_j) \{ [a_{\delta_N}(\theta, \phi_i) - a_{\delta_N}(\theta, \phi_j)] \mathbf{r}_{\delta_N} \\ &\quad + [a_{\delta_T}(\theta, \phi_i) - a_{\delta_T}(\theta, \phi_j)] \mathbf{r}_{\delta_T} \}, \end{aligned} \quad (15)$$

where ϕ_i and ϕ_j denote the i th and j th azimuth angles, respectively, and

$$\overline{\mathbf{W}}(\theta, \phi_i, \phi_j) = \frac{1}{2} (\mathbf{W}(\theta, \phi_i) + \mathbf{W}(\theta, \phi_j)), \quad (16)$$

and \mathbf{r}_{δ_N} and \mathbf{r}_{δ_T} denote the reflection ratio vectors of the fracture weaknesses, given by

$$\begin{aligned} \mathbf{r}_{\delta_N} &= [r_{\delta_N}(1), r_{\delta_N}(2), \dots, r_{\delta_N}(i), \dots, r_{\delta_N}(N)]^T, \\ \mathbf{r}_{\delta_T} &= [r_{\delta_T}(1), r_{\delta_T}(2), \dots, r_{\delta_T}(i), \dots, r_{\delta_T}(N)]^T. \end{aligned} \quad (17)$$

Then, we expand the P-P wave approximation (equation 10) as a Taylor series around the dominant frequency (f_{dom}) of the seismic data as

$$\mathbf{R}_{PP}(\theta, \phi, f_i) \approx \mathbf{R}_{PP}(\theta, \phi, f_{\text{dom}}) + (f_i - f_{\text{dom}}) \frac{d}{df} (\mathbf{R}_{PP}(\theta, \phi, f_i)), \quad (18)$$

where f is the frequency, and f_i and f_{dom} denote the arbitrary frequency and dominant frequency of the seismic data, respectively. Because δ_N is frequency dependent, the P-P reflection coefficient

is expressed as a function of frequency and fracture weaknesses. By substituting equation 18 into equation 15, the azimuthal difference seismic data $\mathbf{S}^*(\theta, \Delta\phi_{ij})$ is rewritten as

$$\begin{aligned} \mathbf{S}^*(\theta, \Delta\phi_{ij}, f_i) &\approx \mathbf{R}_{PP}(\theta, \Delta\phi_{ij}, f_{\text{dom}}) \overline{\mathbf{W}}(\theta, \phi_i, \phi_j, f_i) \\ &\quad + \overline{\mathbf{W}}(\theta, \phi_i, \phi_j, f_i) (f_i - f_{\text{dom}}) \left\{ [a_{\delta_N}(\theta, \phi_i) - a_{\delta_N}(\theta, \phi_j)] \frac{d\mathbf{r}_{\delta_N}}{df} \right. \\ &\quad \left. + [a_{\delta_T}(\theta, \phi_i) - a_{\delta_T}(\theta, \phi_j)] \frac{d\mathbf{r}_{\delta_T}}{df} \right\}, \end{aligned} \quad (19)$$

The iso-frequency seismic component $\mathbf{S}^*(\theta, \Delta\phi_{ij}, f_i)$ can be obtained by applying spectral decomposition to seismic data differentiated by azimuth. To further process the data, we perform a convolution operation on both sides of Equation 19 using a spectral wavelet corresponding to the dominant frequency f_{dom} , i.e., spectral equalization processing, allows the equation to be rederived as

$$\begin{aligned} \mathbf{S}^*(\theta, \Delta\phi_{ij}, f_i) \overline{\mathbf{W}}(\theta, \phi_i, \phi_j, f_{\text{dom}}) - \mathbf{S}^*(\theta, \Delta\phi_{ij}, f_{\text{dom}}) \overline{\mathbf{W}}(\theta, \phi_i, \phi_j, f_i) \\ \approx \overline{\mathbf{W}}(\theta, \phi_i, \phi_j, f_i) \overline{\mathbf{W}}(\theta, \phi_i, \phi_j, f_{\text{dom}}) (f_i - f_{\text{dom}}) \left\{ [a_{\delta_N}(\theta, \phi_i) \right. \\ \left. - a_{\delta_N}(\theta, \phi_j)] \frac{d\mathbf{r}_{\delta_N}}{df} + [a_{\delta_T}(\theta, \phi_i) - a_{\delta_T}(\theta, \phi_j)] \frac{d\mathbf{r}_{\delta_T}}{df} \right\}, \end{aligned} \quad (20)$$

and it can be simply expressed as

$$\mathbf{d} = \mathbf{G}\mathbf{m}, \quad (21)$$

where

$$\begin{aligned} \mathbf{d} &= \mathbf{S}^*(\theta, \Delta\phi_{ij}, f_i) \overline{\mathbf{W}}(\theta, \phi_i, \phi_j, f_{\text{dom}}) \\ &\quad - \mathbf{S}^*(\theta, \Delta\phi_{ij}, f_{\text{dom}}) \overline{\mathbf{W}}(\theta, \phi_i, \phi_j, f_i), \\ \mathbf{G} &= \overline{\mathbf{W}}(\theta, \phi_i, \phi_j, f_i) \overline{\mathbf{W}}(\theta, \phi_i, \phi_j, f_{\text{dom}}) (f_i - f_{\text{dom}}) \\ &\quad [a_{\delta_N}(\theta, \phi_i) - a_{\delta_N}(\theta, \phi_j), a_{\delta_T}(\theta, \phi_i) - a_{\delta_T}(\theta, \phi_j)], \\ \mathbf{m} &= \left[\frac{d\mathbf{r}_{\delta_N}}{df}, \frac{d\mathbf{r}_{\delta_T}}{df} \right]^T. \end{aligned} \quad (22)$$

The frequency-dependent anisotropic parameters can be obtained with the least-squares solution:

$$\mathbf{m} = (\mathbf{G}^T \mathbf{G})^{-1} \mathbf{G}^T \mathbf{d}. \quad (23)$$

The workflow of the proposed frequency-dependent AVAZ inversion for fracture weakness dispersion is shown in Figure 3. First, the smoothed pseudo Wigner-Ville distribution (SPWVD) method is applied to transform the real data into the time-frequency domain. Second, we use a fast Fourier transform (FFT) to obtain the wavelet in the frequency domain. Finally, time-frequency maps obtained in the first step and frequency-domain wavelet obtained in the second step are used to compute the fracture weakness dispersion thanks to the frequency-dependent AVAZ inversion.

AZIMUTHAL REFLECTIVITY ANALYSIS

In this section, the exact solution, the approximation (equation 10), and anisotropic reflectivity methods are applied to simulate azimuthal seismic data. They are also used to verify the accuracy of the reflection coefficients. The approximated one (equation 10) makes use of the linear approximation (equation 10) and assumes weak reflection and anisotropy. We consider the exact solution based on the extended Zoeppritz equation (Schoenberg and Protazio, 1992), which is given in Appendix B. The reflection coefficients are computed by using the properties provided in Table 2. Figure 4 shows the simulation results for the exact and approximate reflection coefficients for the case of a single interface.

The results show that there is a small difference between the approximate and exact results at near incidence angles. We have extracted the AVAZ reflection coefficients for an azimuth angle of 0° and AVAZ reflection coefficients for an incidence angle of 30° and then compared them with the AVAZ reflection coefficients obtained with the exact solution and anisotropic reflectivity method (Figure 5). Although the trend of the AVAZ response is approximately the same at far angles, there is a significant difference between the reflection coefficients. Moreover, we compare the results of the anisotropic reflectivity method with the reflection coefficients

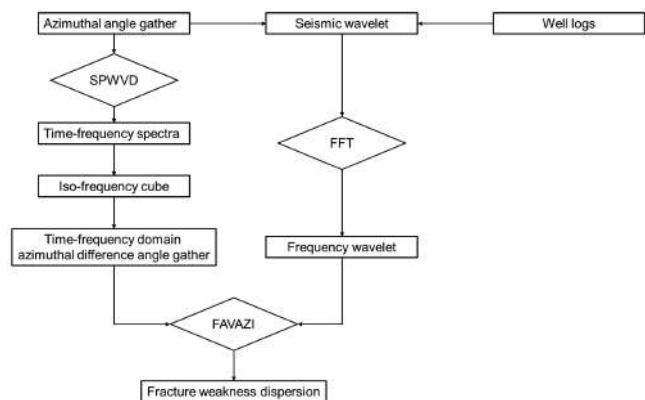


Figure 3. Workflow of the proposed method. FAVAZI: frequency-dependent AVAZ inversion.

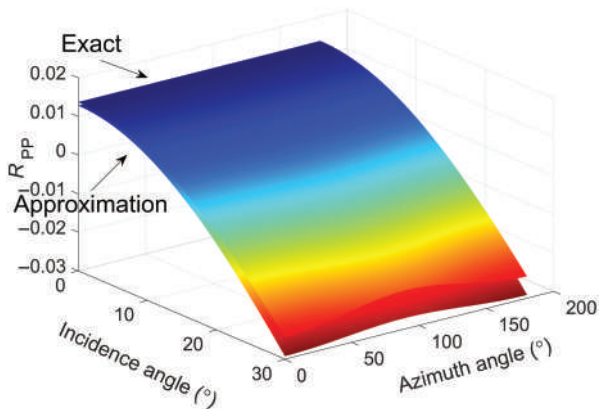


Figure 4. Exact and approximate reflection coefficients as a function of the incidence and azimuth angles for the case of a single interface.

obtained with the exact equation, which shows that they give the same results for the case of the two-layer medium. In essence, the anisotropic reflectivity method is equivalent to the exact equation approach in the case of a single interface. Next, we will apply the exact equation as a forward operator to simulate the AVAZ responses of fractures under different filling conditions.

Mineral filling

Substituting the model properties from Table 3 into equation A-2, we obtain the fracture weaknesses that vary with the P-wave modulus of the filling materials (Figure 6). Fracture weakness decreases

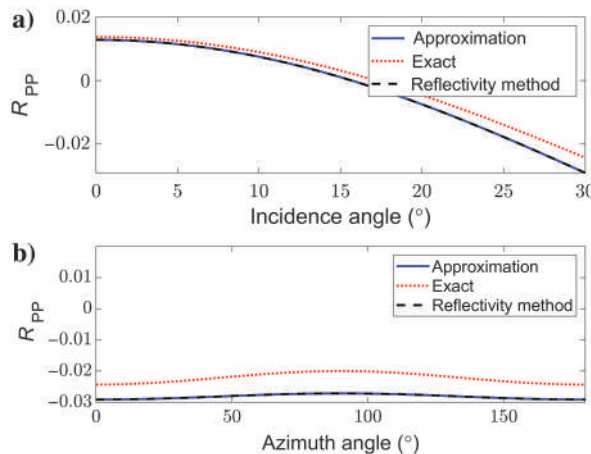


Figure 5. Comparison of AVAZ reflection coefficients by using the approximation and the exact solution, for (a) the 0° azimuth angle and (b) 30° degree incidence angle.

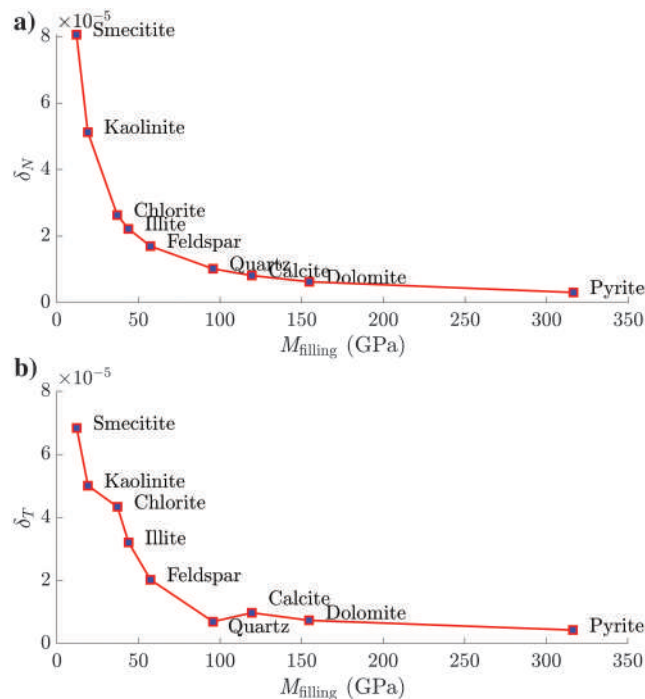


Figure 6. Real part of fracture weaknesses as a function of the P-wave modulus of the fracture filling minerals.

when the fractures are filled with a mineral rather than a fluid by approximately 10^{-5} . Fracture weakness indicates fracture deformation under load. When the fracture is filled with minerals, its strength increases, which in turn reduces the fracture-induced anisotropic characteristics. As the strength of the fracture fillings increases, the weak points of the fracture decrease exponentially and consequently the degree of anisotropy decreases. Therefore, fractures are less prone to deformation when filled with minerals, especially hard minerals, such as pyrite, quartz, and calcite.

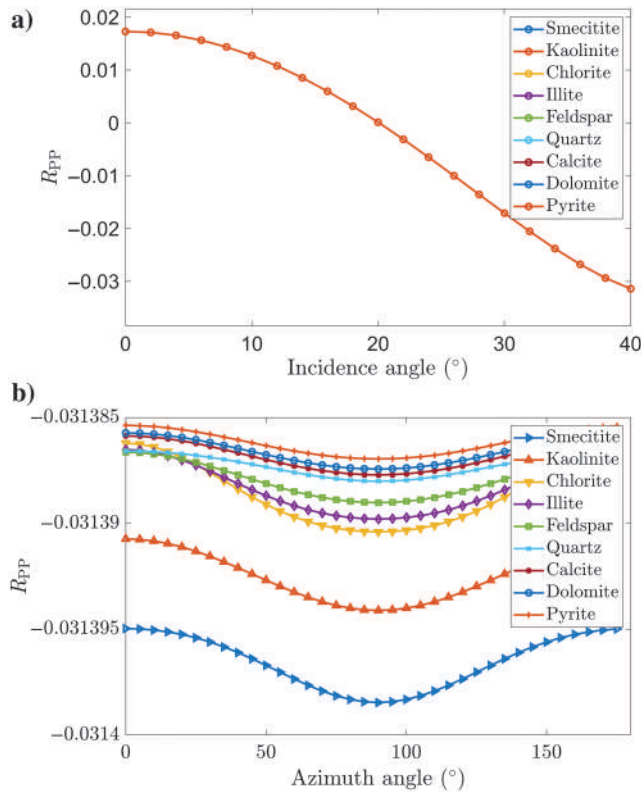


Figure 7. Azimuth-angle-dependent reflection coefficients as a function of the (a) incidence and (b) azimuth angles for different fracture filling minerals by using the extended Zoeppritz equation. Note that reflection coefficients of different minerals exhibit identical curves at the same incidence angle.

The obtained fracture weaknesses are substituted into the stiffness matrix of the two-layer medium. The properties of this medium are shown in Table 2. The upper layer corresponds to an isotropic medium and the lower layer to an HTI medium containing fractures. Then, we extend the Zoeppritz equation to model the reflection coefficient, as shown in Figure 7. The plot shows that there is a negligible difference from a practical point of view when the pore infill is a mineral.

Fluid filling

In the case of fractured reservoirs, the fractures might serve as storage spaces for natural gas in addition to filling with minerals. Using the same method, we filled the fractures with mixed fluids with different gas saturations and observed the changes of fracture weakness parameters. Compared with mineral filled, fluid-filled fractures exhibit more pronounced anisotropy. The fracture weakness δ_N is influenced by the volume proportion of gas q_g and the frequency f , as shown in Figure 8. Figure 9 highlights the specific case of 30 Hz, demonstrating that the frequency-dependent dispersion induced by gas becomes particularly significant at

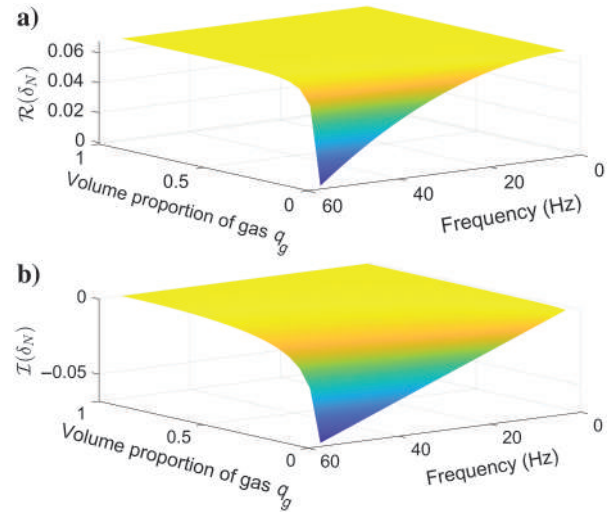


Figure 8. (a) Real part $R(\delta_N)$ and (b) imaginary part $I(\delta_N)$ of the normal fracture weakness as a function of frequency and volume proportion of gas for fluid-bearing fractured rocks.

Table 3. Elastic properties of the minerals.

Minerals	M_b (GPa)	μ_b (GPa)	ρ (g/cm ³)	Reference	
Clay	Illite	43.92	9.21	2.55	Eastwood and Castagna (1987)
	Smectite	12.10	3.87	2.29	Vanorio et al. (2003)
	Kaolinite	19.02	5.98	2.59	Vanorio et al. (2003)
	Chlorite	37.09	7.18	2.69	Wang et al. (2001) and Hui et al. (2011)
Brittle	Quartz	95.65	44.01	2.65	Carmichael (1988)
	Feldspar	57.38	14.97	2.62	Mavko et al. (2020)
	Calcite	119.48	32.07	2.71	Simmons (1965)
	Dolomite	154.62	45.01	2.87	Humbert and Plique (1972)
	Pyrite	316.39	132.28	4.93	Simmons and Birch (1963)

low gas saturations. As q_g increases, the two parts increase, while the slope of each part with respect to q_g gradually decreases. The cases of $q_g = 25\%$, 50% , and 75% are also extracted and shown in Figure 10. The higher frequency results yield stronger dispersion, especially when the saturation is low. There is sensitivity of AVO to gas saturation and frequency.

Subsequently, the established stiffness coefficient matrix is used to simulate the variation of seismic reflectivity with respect to incidence and azimuth angle. Figures 11 and 12 show the P-P reflection coefficient as a function of frequency and q_g for (a) increasing angle of incidence with constant azimuth angle of 0° (Figures 11a and 12a) and (b) increasing azimuth angle with constant incidence angle of 40° (Figures 11b and 12b). Note that the reflection coefficient varies significantly with frequency, setting the basis for the differentiation between mineral-filled and liquid-filled fractures using frequency-dependent properties. In addition, simulations can be performed for different q_g values, which affect the magnitude of the AVAZ reflection coefficient, with the coefficient varying more significantly as the fractures contain more gas. The fracture filling fluid causes dispersion of the seismic response, which can be applied to identify gas-bearing fractures.

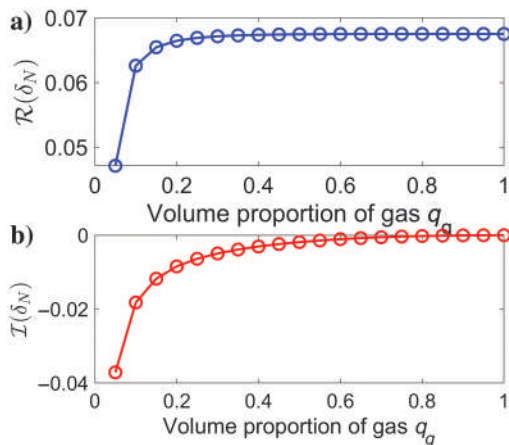


Figure 9. Extracted (a) real part $R(\delta_N)$ and (b) imaginary part $I(\delta_N)$ of the normal fracture weakness at 30 Hz.

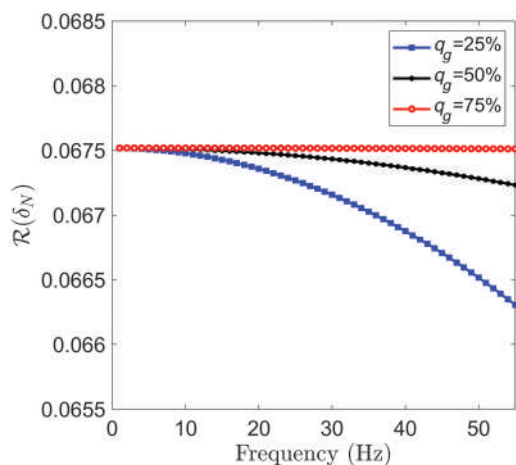


Figure 10. Extracted real part $R(\delta_N)$ of the normal fracture weakness at $q_g = 25\%$, 50% , and 75% .

REAL SEISMIC-DATA APPLICATION

The frequency-dependent AVAZ inversion method is used on field data acquired in the Luzhou area in the southern Sichuan basin, southwest China. A series of relatively tight anticlines and wide and gentle synclines are present with an echelon in the north–south direction. The uplift is an asymmetric anticline, and the sides of the uplift correspond to two depressions. Therefore, a number of fractures have developed, especially at the edge of the uplift. Figure 13 shows the poststack seismic data. The green curve corresponds to the top of a fractured shale reservoir. The reservoir is located in the Longmaxi-Wufeng shale formation at approximately 3500 m deep, and the sediments above and below the reservoir are limestones. Due to the tectonic activity in the area, large fractures have been developed in the shale. Moreover, the fractures all have high tilt angles, and the reservoir is identified as an HTI medium. The data include 500 azimuthal prestack angle gathers, with the azimuth angle ranging from 1° – 180° with an increment of 30° , and the incidence angle ranging from 0° – 30° with an increment of 5° . Well A is located at the 2094th common depth point (CDP), as indicated with the red line in Figure 13.

Figure 14 shows the results of the seismic well tie, which is very important for the seismic-based prediction. The poststack synthetic data are simulated by convolving the reflectivity series with the seismic wavelet. The incidence- and azimuth-angle-dependent wavelets are extracted from the azimuthal angle gather with well-log data. The poststack reflectivity series is

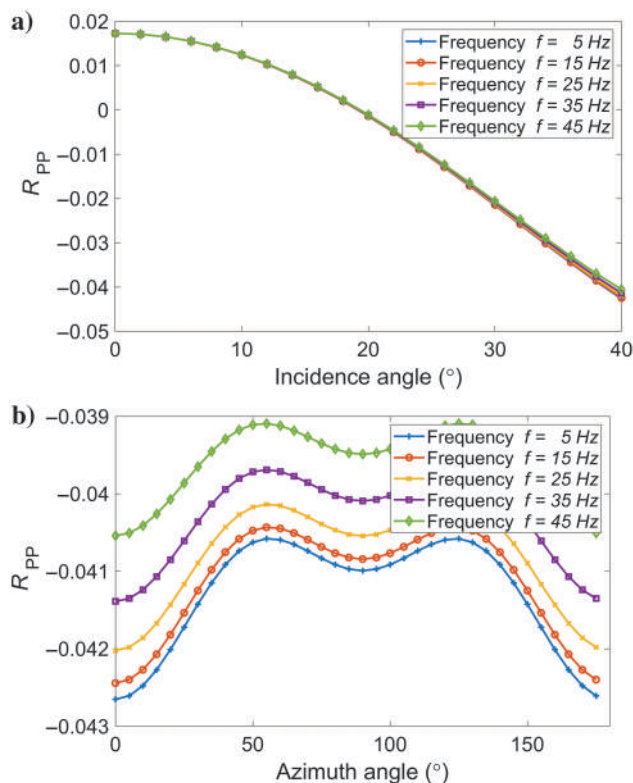


Figure 11. The P-P wave reflection coefficients for different frequencies for (a) increasing incidence angle with constant azimuth angle of 0° and (b) increasing azimuth angle with constant incidence angle of 40° .

$$r = \frac{I_P^d - I_P^u}{I_P^d + I_P^u}, \quad (24)$$

where I_P denotes the P impedance, shown in Figure 14a. Figure 14b and 14c corresponds to the synthetic seismic data and the poststack seismic data, respectively. The seismic well tie is estimated by the dynamic time warping algorithm (Hale, 2013). The P-wave impedance shows a strong increase at the top of the reservoir (approximately 3800 m), and is resolved by the inversion. Figure 15a and 15b shows the real azimuthal angle gather and the simulated synthetic data by using equation 13 with the depth-time correlation of Figure 14.

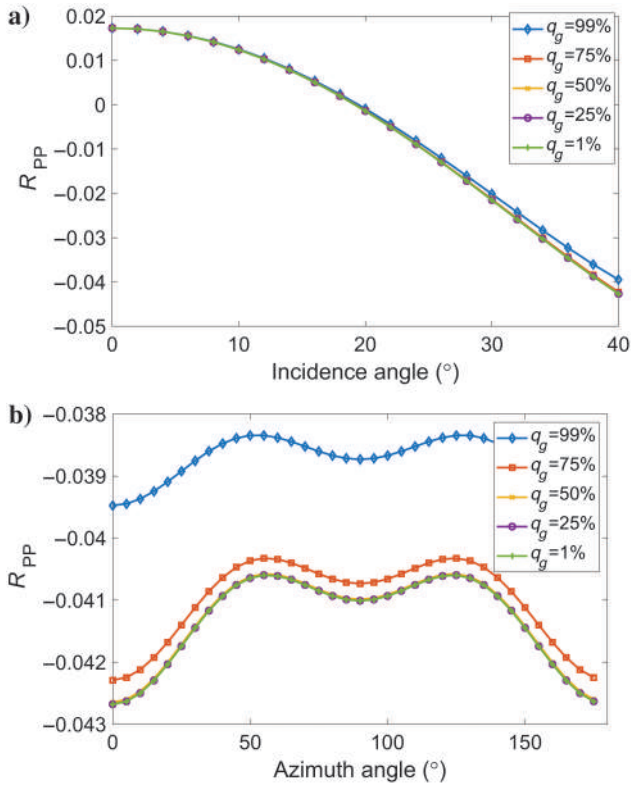


Figure 12. The P-P wave reflection coefficients for different q_g s for (a) increasing incidence angle with constant azimuth angle of 0° and (b) increasing azimuth angle with constant incidence angle of 40° .

The reservoir is located at the lower parts of Figures 14 and 15, and thus we mainly focus on the well-tie results of the lower event.

Figure 16a and 16b shows the extracted partial-stack data along the 0° and 90° azimuth angles, respectively, and the difference between the two profiles is given in Figure 16c. The dashed black lines indicate the location of the reservoir. The gas-bearing area is highlighted in Figure 16 with dashed red lines. A comparison with the difference profile shows that there is a significant fracture-induced azimuthal amplitude difference at the fractured shale reservoir location. We can see that the AVA and AVAZ characteristics of the synthetic data are consistent with the real seismic data.

A spectral decomposition is performed on the azimuthal difference data, to obtain the time-frequency analysis of the seismic traces. A SPWVD method (Auger and Flandrin, 1995) is used to process the data. Figure 17 shows the decomposition results of the 1801 trace for the 0° , 60° , and 90° azimuth angles at an incidence angle of 25° . The strong energy clusters approximately at 1.8–2.0 s correspond to the top of the shale gas reservoir. The seismic data show significant dispersion in the gas reservoir, with the main frequency decreasing from 35 Hz to less than 30 Hz. Figure 18 shows the iso-frequency sections of the azimuthal angle difference data obtained with the SPWVD method at 15, 30, and 45 Hz. The dashed red boxes correspond to the location of the reservoir. The difference between nonreservoir and reservoir areas is small at low frequencies, e.g., 15 Hz. The difference increases when considering high frequencies (30 to 45 Hz),

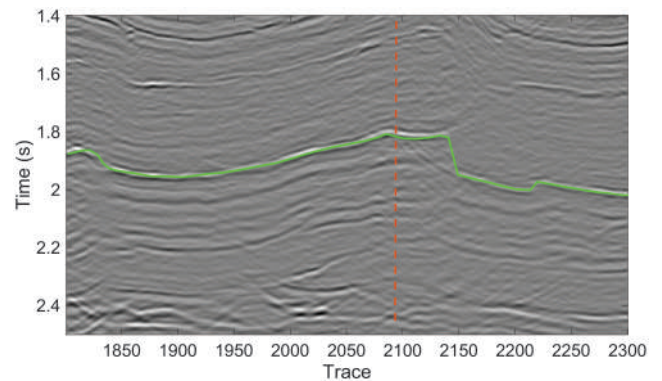


Figure 13. Poststack profile of the real seismic data, where the green curves and red line correspond to the top of a fractured reservoir and well location, respectively.

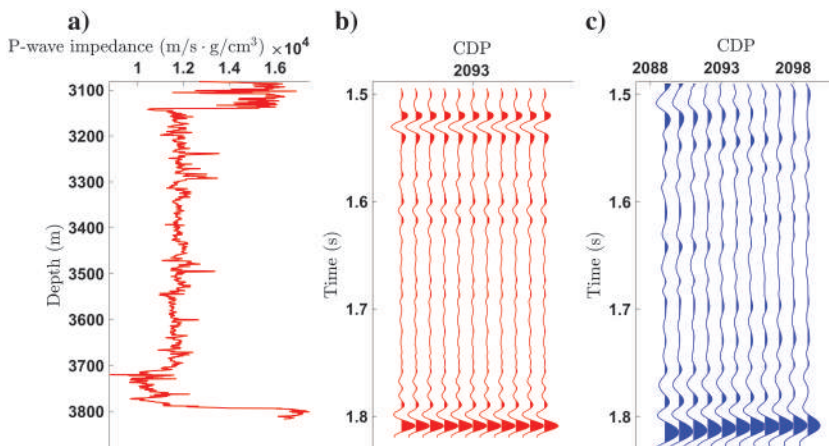


Figure 14. The (a) P-wave impedance seismic data and the duplicated 11 CDP synthetic data by using reflectivity series convolved with (a) the wavelet and (c) the well tie at the well location.

particularly at azimuths of 120° – 30° and 150° – 60° . Figure 19 indicates that a time-frequency analysis reveals the energy loss at high frequencies. However, iso-frequency sections exhibit a poor lateral continuity.

The proposed method has potential limitations in its application. Factors such as coherent or random noise interference, complex distributions of fracture orientations, and the intrinsic heterogeneity of geologic formations may affect the precision and reliability of inversion results. In addition, certain assumptions of the model, such as homogeneity within each fracture zone, might not be reasonable in describing the formations with stronger heterogeneity or anisotropy, thus potentially affecting the result of fluid detection.

Finally, the inversion method, in equation 23, is applied to extract the dispersion of the fracture weakness, dr_{δ_N}/df . Here, we only use the data within the seismic frequency band (5–50 Hz) for inversion, minimizing the influence of other factors (such as noise) on the dispersion inversion. As shown in Figure 19, the fracture weakness dispersion, as an appropriate fluid indicator, is well adapted to shale-gas reservoirs. Due to the presence of shale gas, significant dispersion occurs, mainly related to the fracture weakness parameter, as demonstrated by the proposed method.

To further verify the effectiveness of the proposed method, Figure 20 shows inverted fracture weakness dispersion and a water-saturation well-log profile. The target reservoir is located approximately at 1.8 s at the well location. The water saturation at the reservoir ranges between 70% and 80%, which means that the gas saturation of fractured gas-bearing reservoir is approximately 25%. As shown in Figures 8–10, the gas in fractures can induce an apparent dispersion

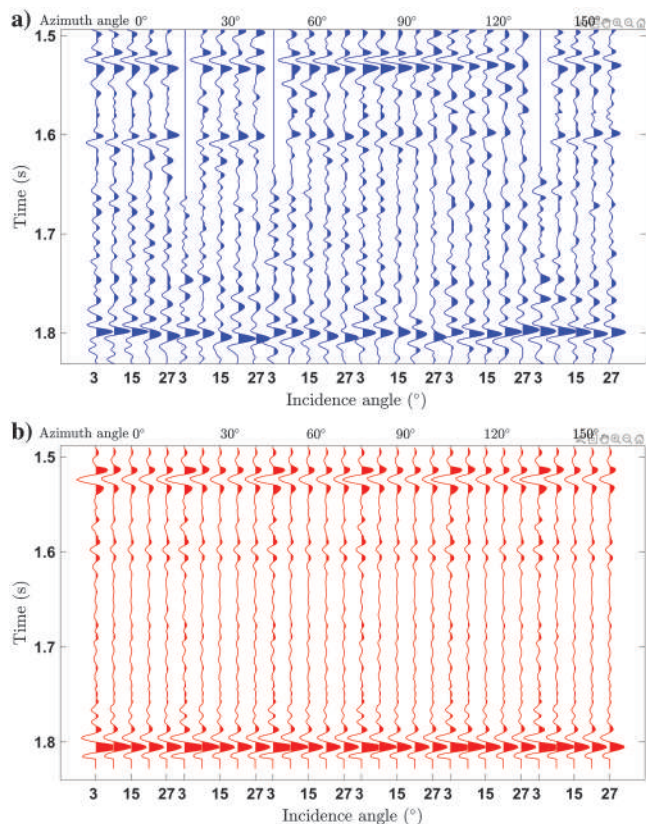


Figure 15. The (a) real azimuthal angle gather and (b) the simulated synthetic data by using the depth-time correlation in Figure 13.

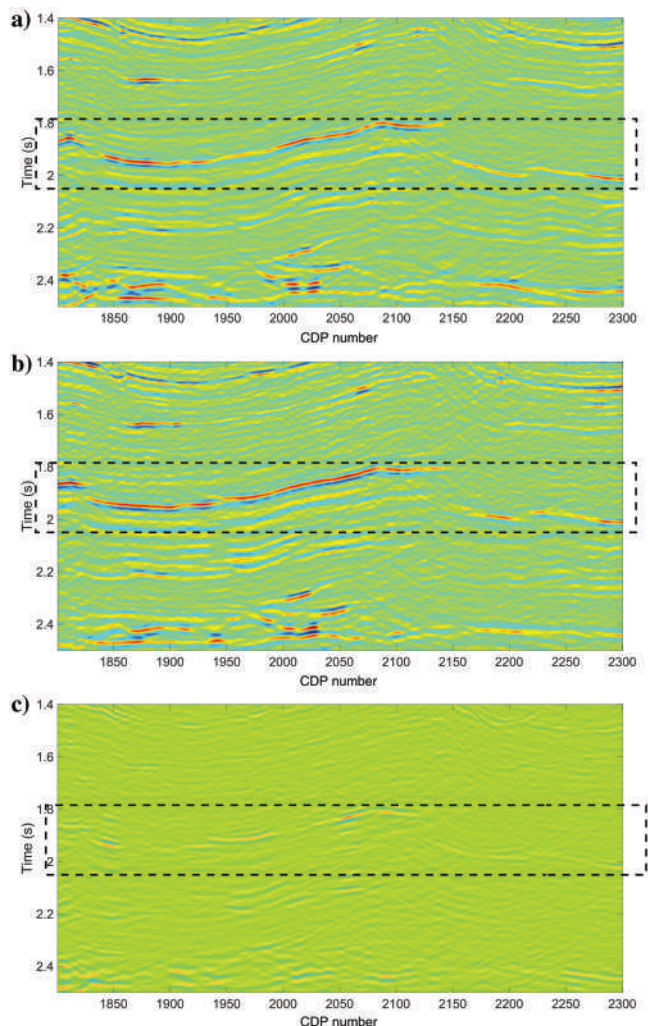


Figure 16. Extracted partial-stack seismic data along (a) 0° and (b) 90° azimuth angles, and (c) the difference between the two profiles. The dashed black lines correspond to the location of the fractured reservoir.

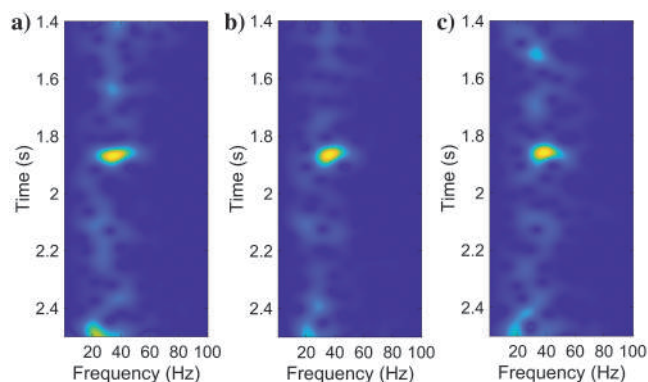


Figure 17. Spectral decomposition of the 1801 trace for (a) 0° , (b) 60° , and (c) 90° azimuth angles at an incidence angle of 25° .

feature, which can be used to estimate fluid properties. Low water saturation (high gas content) is correlated with high-frequency dispersion. The real seismic data application demonstrates that the proposed method can be adopted for fractured reservoir characterization and fluid detection.

CONCLUSION

Fracture weaknesses, in particular the normal fracture weakness, are strongly frequency-dependent parameters when they are saturated with gas. The dispersion of the fracture weakness is an important factor in indicating the type of fluid. Introducing an effective model for wave dispersion and considering a cracked rock with different fracture filling materials, we analyze the P-P wave reflection coefficients as a function of frequency and fluid properties. Our analysis reveals that the normal fracture weakness exhibits considerable dispersion, i.e., frequency dependence, when the fractures are filled with gas. We propose a frequency-dependent AVAZ inversion method for characterizing the fracture infills, leveraging the wave dispersion to improve the accuracy of fluid identification. The proposed methodology is effectively applied to field data, providing a new approach for identifying fluid types and improving subsurface characterization.

The proposed method has demonstrated its effectiveness in improving subsurface medium characterization and identifying fluid types. However, potential limitations, such as noise interference, geologic heterogeneity, and variations in fracture orientations and distributions, may affect its performance. Addressing these limitations in future work could enhance its applicability under various field conditions.

ACKNOWLEDGMENTS

This work was supported in part by the National Science and Technology Major Project of China under grant no. 2024ZD1004300, in part by the National Natural Science Foundation of China under grant no. 42304133, and in part by the Key Project from the Hubei Research Center for Basic Disciplines of Earth Sciences under grant no. HRCES-202401.

DATA AND MATERIALS AVAILABILITY

Data associated with this research are confidential and cannot be released.

APPENDIX A

FREQUENCY-DEPENDENT STIFFNESS MATRIX OF THE HTI MEDIUM

According to the Schoenberg model (Schoenberg and Sayers, 1995), the normal and tangential weaknesses are

$$\delta_N = U_{33}e, \quad \delta_T = U_{11}e. \quad (A-1)$$

The fractures may be filled with the different types of fillings, such as gas, oil or water, or mineral components. However, in deep fractured shales, a number of paleo fractures may be filled with minerals, as a result of long-term geologic effects. In the case of mineral-filled fractures, the WIFF effect is not important and we neglect the associated relaxation time. In such cases, U_{11} and U_{33} are

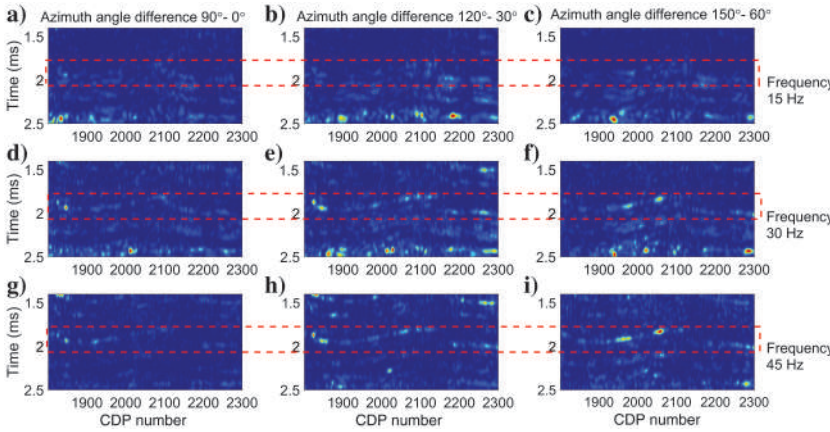


Figure 18. Iso-frequency sections of azimuth angle difference data obtained by the SPWVD method at (a-c) 15, (d-f) 30, and (g-i) 45 Hz.

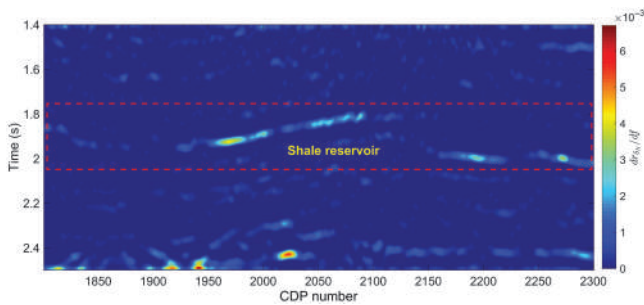


Figure 19. Fracture weakness dispersion estimated with the proposed inversion method.

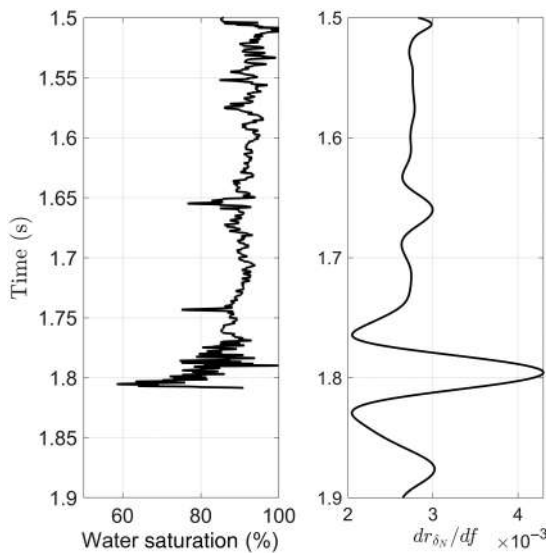


Figure 20. (a) Water saturation well-log curve and (b) fracture weakness dispersion.

$$U_{11} = \frac{16}{3(3-2g)} \frac{1}{1 + \frac{4}{\pi(3-2g)} \frac{\mu'}{\mu_b \chi}},$$

$$U_{33} = \frac{4}{3g(1-g)} \frac{1}{1 + \frac{1}{\pi(1-g)} \frac{K' + (4\mu'/3)}{\mu_b \chi}}, \quad (\text{A-2})$$

, where $g = \mu_b/M_b$, χ is the aspect ratio of the fractures, and K' and μ' denote the bulk and shear moduli of the fracture fillings, respectively, which are frequency independent.

Variations with frequency need to be accounted for if the fractures are partially fluid saturated. For fluid-filled fractures, equation A-2 is not valid because of the presence of the loss mechanism. According to the modified Hudson model (Pointer et al., 2000), U_{11} and U_{33} for partially saturated fractures considering the WIFF effect are

$$U_{11} \approx \frac{16}{3(3-2g)}, \quad U_{33} \approx \frac{4}{3g(1-g)} (1 - \omega^2 \Gamma^2 - i\omega\Gamma), \quad (\text{A-3})$$

where $i = \sqrt{-1}$, ω is the angular frequency, and Γ are relaxation times along the spatial axes x_3 , given by

$$\Gamma = \frac{1}{\pi\mu(1-g)\chi^3} \frac{\eta_l F_l(q_l)}{(1-q_l)^2}, \quad (\text{A-4})$$

where

$$F_l(q_l) = 0.053(1-q_l)[1 + \cos \pi(1-q_l)], \quad (\text{A-5})$$

and q_l denotes the volume proportions of liquid, and η_l is the corresponding viscosity. According to Bakulin et al. (2000a, 2000b),

$$\delta_N^{\text{dry}} = \frac{4e}{3g(1-g)}, \quad \delta_T^{\text{dry}} = \frac{16e}{3(3-2g)} \quad (\text{A-6})$$

are the normal and tangential weaknesses of the dry fractures, respectively. Thus, by combining equation A-6 into equation A-5, we obtain

$$U_{11} = \delta_T^{\text{dry}}/e, \quad U_{33} = \delta_N^{\text{dry}}/e - (\omega^2 \Gamma^2 + i\omega\Gamma) \delta_N^{\text{dry}}/e. \quad (\text{A-7})$$

As shown in equation A-7, the U_{33} can be considered with two parts, i.e., related to the dry-fracture part $U_{33}^1 = \delta_N^{\text{dry}}/e$ and fluid-induced dispersion part $U_{33}^2 = -(\omega^2 \Gamma^2 + i\omega\Gamma) \delta_N^{\text{dry}}/e$. It is shown that U_{33}^2 is not completely decoupled, and δ_N^{dry} still affects U_{33}^2 . Here, we neglect the effect and attribute it to the fluid-related term U_{33}^2 . Then, substituting U_{11} and U_{33} into the stiffness matrix gives

$$\mathbf{C} = \mathbf{C}_b + \mathbf{C}_{\text{crack}} + \mathbf{C}_{\text{fluid}}, \quad (\text{A-8})$$

where

$$\mathbf{C}_b = \begin{bmatrix} M_b & \lambda_b & \lambda_b & 0 & 0 & 0 \\ \lambda_b & M_b & \lambda_b & 0 & 0 & 0 \\ \lambda_b & \lambda_b & M_b & 0 & 0 & 0 \\ 0 & 0 & 0 & \mu_b & 0 & 0 \\ 0 & 0 & 0 & 0 & \mu_b & 0 \\ 0 & 0 & 0 & 0 & 0 & \mu_b \end{bmatrix}, \quad (\text{A-9})$$

$$\mathbf{C}_{\text{crack}} = - \begin{bmatrix} \frac{M_b \delta_N^{\text{dry}}}{g} & \frac{\lambda_b \delta_N^{\text{dry}}}{g} & \frac{\lambda_b \delta_N^{\text{dry}}}{g} & 0 & 0 & 0 \\ \frac{\lambda_b \delta_N^{\text{dry}}}{g} & \frac{\lambda_b^2 \delta_N^{\text{dry}}}{\mu} & \frac{\lambda_b \delta_N^{\text{dry}}}{g} & 0 & 0 & 0 \\ \frac{\lambda_b \delta_N^{\text{dry}}}{g} & \frac{\lambda_b \delta_N^{\text{dry}}}{g} & \frac{\lambda_b^2 \delta_N^{\text{dry}}}{\mu} & 0 & 0 & 0 \\ 0 & 0 & 0 & 0 & \delta_T^{\text{dry}} & 0 \\ 0 & 0 & 0 & 0 & 0 & \delta_T^{\text{dry}} \end{bmatrix}, \quad (\text{A-10})$$

and

$$\mathbf{C}_{\text{fluid}} = (\omega^2 \Gamma^2 + i\omega\Gamma) \begin{bmatrix} \frac{M_b \delta_N^{\text{dry}}}{g} & \frac{\lambda_b \delta_N^{\text{dry}}}{g} & \frac{\lambda_b \delta_N^{\text{dry}}}{g} & 0 & 0 & 0 \\ \frac{\lambda_b \delta_N^{\text{dry}}}{g} & \frac{\lambda_b^2 \delta_N^{\text{dry}}}{\mu} & \frac{\lambda_b \delta_N^{\text{dry}}}{g} & 0 & 0 & 0 \\ \frac{\lambda_b \delta_N^{\text{dry}}}{g} & \frac{\lambda_b \delta_N^{\text{dry}}}{g} & \frac{\lambda_b^2 \delta_N^{\text{dry}}}{\mu} & 0 & 0 & 0 \\ 0 & 0 & 0 & 0 & 0 & 0 \\ 0 & 0 & 0 & 0 & 0 & 0 \\ 0 & 0 & 0 & 0 & 0 & 0 \end{bmatrix}. \quad (\text{A-11})$$

The stiffness matrix of rocks with partially saturated fractures is frequency dependent, and the ratio of the imaginary and real parts of matrix varies with frequency, fluid saturation, fracture aspect ratio, and fracture density.

In the presence of weak anisotropy, the stiffness components c_{ijkl} at a weak-contrast interface can be considered to be perturbed on the basis of a reference (or background) medium. Thus, the real and imaginary parts of the perturbation are

$$R[\Delta\mathbf{C}(\omega)] = - \begin{bmatrix} (1-\omega^2 \Gamma^2) \frac{M_b \delta_N^{\text{dry}}}{g} & (1-\omega^2 \Gamma^2) \frac{\lambda_b \delta_N^{\text{dry}}}{g} & (1-\omega^2 \Gamma^2) \frac{\lambda_b \delta_N^{\text{dry}}}{g} & 0 & 0 & 0 \\ (1-\omega^2 \Gamma^2) \frac{\lambda_b \delta_N^{\text{dry}}}{g} & (1-\omega^2 \Gamma^2) \frac{\lambda_b^2 \delta_N^{\text{dry}}}{\mu} & (1-\omega^2 \Gamma^2) \frac{\lambda_b \delta_N^{\text{dry}}}{g} & 0 & 0 & 0 \\ (1-\omega^2 \Gamma^2) \frac{\lambda_b \delta_N^{\text{dry}}}{g} & (1-\omega^2 \Gamma^2) \frac{\lambda_b \delta_N^{\text{dry}}}{g} & (1-\omega^2 \Gamma^2) \frac{\lambda_b^2 \delta_N^{\text{dry}}}{\mu} & 0 & 0 & 0 \\ 0 & 0 & 0 & 0 & 0 & 0 \\ 0 & 0 & 0 & 0 & \delta_T^{\text{dry}} & 0 \\ 0 & 0 & 0 & 0 & 0 & \delta_T^{\text{dry}} \end{bmatrix},$$

$$I[\Delta\mathbf{C}(\omega)] = \omega\Gamma \begin{bmatrix} \frac{M_b \delta_N^{\text{dry}}}{g} & \frac{\lambda_b \delta_N^{\text{dry}}}{g} & \frac{\lambda_b \delta_N^{\text{dry}}}{g} & 0 & 0 & 0 \\ \frac{\lambda_b \delta_N^{\text{dry}}}{g} & \frac{\lambda_b^2 \delta_N^{\text{dry}}}{\mu} & \frac{\lambda_b \delta_N^{\text{dry}}}{g} & 0 & 0 & 0 \\ \frac{\lambda_b \delta_N^{\text{dry}}}{g} & \frac{\lambda_b \delta_N^{\text{dry}}}{g} & \frac{\lambda_b^2 \delta_N^{\text{dry}}}{\mu} & 0 & 0 & 0 \\ 0 & 0 & 0 & 0 & 0 & 0 \\ 0 & 0 & 0 & 0 & 0 & 0 \\ 0 & 0 & 0 & 0 & 0 & 0 \end{bmatrix}. \quad (\text{A-12})$$

APPENDIX B

AZIMUTHAL SEISMIC-DATA SIMULATION

We consider the two homogeneous arbitrarily anisotropic half-spaces separated by a planar interface. The two half-spaces are characterized by the densities ρ^1, ρ^2 and the stiffness tensor components c_{ijkl}^1, c_{ijkl}^2 . By assuming that P waves impinge at normal incidence from the upper half-space to the interface, reflected and transmitted P, S1, and S2 waves are generated, whose displacement vectors are

$$\mathbf{u}^n(x, t) = U^n \mathbf{p}^n \exp[-i\omega(t - \mathbf{s}^n \cdot \mathbf{x})], \quad (\text{B-1})$$

where U is the scalar amplitude; $i = \sqrt{-1}$; t is the propagation time of the seismic wave at a distance x ; $n = 0$ denotes the incidence wave; $n = 1, 2, 3$ correspond to the reflected S_1 , S_2 , and P waves, and $n = 4, 5, 6$ are the corresponding transmitted waves, respectively; and \mathbf{p}^n and \mathbf{s}^n are the polarization and slowness vectors, which can be obtained by solving the Christoffel equation (Ali and Jakobsen, 2011, 2014):

$$(\mathbf{Y} - \rho \mathbf{I})\mathbf{P} = 0, \quad (\text{B-2})$$

where \mathbf{I} is the identity diagonal matrix, and equation B-2 can be specified as

$$\begin{bmatrix} \Upsilon_{11} - \rho & \Upsilon_{12} & \Upsilon_{13} \\ \Upsilon_{21} & \Upsilon_{22} - \rho & \Upsilon_{23} \\ \Upsilon_{31} & \Upsilon_{32} & \Upsilon_{33} - \rho \end{bmatrix} \begin{bmatrix} p_1 \\ p_2 \\ p_3 \end{bmatrix} = 0, \quad (\text{B-3})$$

where Υ_{ij} is obtained from the generalized Hooke's law:

$$\begin{aligned} \Upsilon_{11} &= c_{11}s_1^2 + c_{66}s_2^2 + c_{55}s_3^2 + 2c_{16}s_1s_2, \\ \Upsilon_{22} &= c_{66}s_1^2 + c_{22}s_2^2 + c_{44}s_3^2 + 2c_{26}s_1s_2, \\ \Upsilon_{33} &= c_{55}s_1^2 + c_{44}s_2^2 + c_{33}s_3^2 + 2c_{45}s_1s_2, \\ \Upsilon_{12} = \Upsilon_{21} &= (c_{12} + c_{66})s_1s_2 + (c_{66} + c_{12})s_1s_2, \\ \Upsilon_{13} = \Upsilon_{31} &= (c_{13} + c_{55})s_1s_3 + (c_{36} + c_{45})s_2s_3, \\ \Upsilon_{23} = \Upsilon_{32} &= (c_{23} + c_{44})s_2s_3 + (c_{36} + c_{45})s_1s_3. \end{aligned} \quad (\text{B-4})$$

Then, with the given incidence and azimuth angles, the horizontal slownesses s_1 and s_2 are

$$s_1 = \frac{\sin \theta \cos \phi}{\sqrt{c_{11}/\rho}}, \quad s_2 = \frac{\sin \theta \sin \phi}{\sqrt{c_{11}/\rho}}. \quad (\text{B-5})$$

The vanishing determinant $\det(\mathbf{Y} - \rho \mathbf{I}) = 0$ gives the solutions of the vertical slowness s_3 with associated polar vectors \mathbf{p} .

Schoenberg and Protazio (1992) rationalize and generalize the Zoeppritz equation to the anisotropic case, which gives the exact solution of the reflection and transmission coefficients. The reflectivity coefficient matrix is given by

$$\begin{aligned} \mathbf{R} &= (\mathbf{Y}'^{-1}\mathbf{Y} + \mathbf{X}'^{-1}\mathbf{X})^{-1}(\mathbf{Y}'^{-1}\mathbf{Y} - \mathbf{X}'^{-1}\mathbf{X}) \\ &= \begin{bmatrix} R_{PP} & R_{SP} & R_{TP} \\ R_{PS} & R_{SS} & R_{TS} \\ R_{PT} & R_{ST} & R_{TT} \end{bmatrix}, \end{aligned} \quad (\text{B-6})$$

where

$$\mathbf{X} = \begin{bmatrix} e_{P_1} & e_{S_1} & e_{T_1} \\ e_{P_2} & e_{S_2} & e_{T_2} \\ -(c_{13}e_{P_1} + c_{36}e_{P_2})s_1 & -(c_{13}e_{S_1} + c_{36}e_{S_2})s_1 & -(c_{13}e_{T_1} + c_{36}e_{T_2})s_1 \\ -(c_{23}e_{P_2} + c_{36}e_{P_1})s_2 & -(c_{23}e_{S_1} + c_{36}e_{S_2})s_2 & -(c_{23}e_{T_2} + c_{36}e_{T_1})s_2 \\ -c_{33}s_3p_3 & -c_{33}s_3s_3 & -c_{33}s_3e_{T_3} \end{bmatrix}, \quad (\text{B-7})$$

$$\mathbf{Y} = \begin{bmatrix} -(c_{55}s_1 + c_{45}s_2)e_{P_3} & -(c_{55}s_1 + c_{45}s_2)e_{S_3} & -(c_{55}s_1 + c_{45}s_2)e_{T_3} \\ -(c_{55}e_{P_1} + c_{45}e_{P_2})s_{3p} & -(c_{55}e_{S_1} + c_{45}e_{S_2})s_{3s} & -(c_{55}e_{T_1} + c_{45}e_{T_2})s_{3t} \\ -(c_{45}s_1 + c_{44}s_2)e_{P_3} & -(c_{45}s_1 + c_{44}s_2)e_{S_3} & -(c_{45}s_1 + c_{44}s_2)e_{T_3} \\ -(c_{45}e_{P_1} + c_{44}e_{P_2})s_{3p} & -(c_{45}e_{S_1} + c_{44}e_{S_2})s_{3s} & -(c_{45}e_{T_1} + c_{44}e_{T_2})s_{3t} \\ e_{P_3} & e_{S_3} & e_{T_3} \end{bmatrix}, \quad (\text{B-8})$$

where \mathbf{e} is the polar vector obtained by solving the Christoffel equations (Aki and Richards, 1980), the subscripts $\{\cdot\}_P$, $\{\cdot\}_S$, and $\{\cdot\}_T$ denote the P, S_1 , and S_2 waves, respectively. The terms \mathbf{X}' and \mathbf{Y}' are the matrix functions of parameters as in equations B-7 and B-8 with primed parameters for the lower transmitting medium. P-P reflected seismic data are considered, which can be expressed as the reflectivity profile convolved with the seismic wavelet:

$$\mathbf{S}(\theta, \phi) = \mathbf{W}(\theta, \phi)\mathbf{R}_{PP}(\theta, \phi) + \mathbf{n}, \quad (\text{B-9})$$

where \mathbf{n} is the noise.

REFERENCES

- Aki, K., and P. G. Richards, 1980, Quantitative seismology: Theory and methods: W. H. Freeman.
- Ali, A., and M. Jakobsen, 2011, Seismic characterization of reservoirs with multiple fracture sets using velocity and attenuation anisotropy data: *Journal of Applied Geophysics*, **75**, 590–602, doi: [10.1016/j.jappgeo.2011.09.003](https://doi.org/10.1016/j.jappgeo.2011.09.003).
- Ali, A., and M. Jakobsen, 2014, Anisotropic permeability in fractured reservoirs from frequency-dependent seismic amplitude versus angle and azimuth data: *Geophysical Prospecting*, **62**, 293–314, doi: [10.1111/1365-2478.12084](https://doi.org/10.1111/1365-2478.12084).
- Auger, F., and P. Flandrin, 1995, Improving the readability of time-frequency and time-scale representations by the reassignment method: *IEEE Transactions on Signal Processing*, **43**, 1068–1089, doi: [10.1109/78.382394](https://doi.org/10.1109/78.382394).
- Ba, J., W. Xu, L. Fu, J. M. Carcione, and L. Zhang, 2017, Rock anelasticity due to patchy-saturation and fabric heterogeneity: A double double-porosity model of wave propagation: *Journal of Geophysical Research: Solid Earth*, **122**, 1949–1976, doi: [10.1002/2016JB013882](https://doi.org/10.1002/2016JB013882).
- Bakulin, A., V. Grechka, and I. Tsvankin, 2000a, Estimation of fracture parameters from reflection seismic data — Part I: HTI model due to a single fracture set: *Geophysics*, **65**, 1788–1802, doi: [10.1190/1.1444863](https://doi.org/10.1190/1.1444863).
- Bakulin, A., V. Grechka, and I. Tsvankin, 2000b, Estimation of fracture parameters from reflection seismic data — Part II: Fractured models with orthorhombic symmetry: *Geophysics*, **65**, 1803–1817, doi: [10.1190/1.1444864](https://doi.org/10.1190/1.1444864).
- Brajanovski, M., B. Gurevich, and M. Schoenberg, 2005, A model for P-wave attenuation and dispersion in a porous medium permeated by aligned fractures: *Geophysical Journal International*, **163**, 372–384, doi: [10.1111/j.1365-246X.2005.02722.x](https://doi.org/10.1111/j.1365-246X.2005.02722.x).
- Carcione, J. M., 2000, A model for seismic velocity and attenuation in petroleum source rocks: *Geophysics*, **65**, 1080–1092, doi: [10.1190/1.1444801](https://doi.org/10.1190/1.1444801).
- Carcione, J. M., 2022, Wave fields in real media: Wave propagation in anisotropic, anelastic, porous and electromagnetic media, 4th ed.: Elsevier.
- Carcione, J. M., and S. Picotti, 2012, Reflection and transmission coefficients of a fracture in transversely isotropic media: *Studia Geophysica et Geodaetica*, **56**, 307–322, doi: [10.1007/s11200-011-9034-4](https://doi.org/10.1007/s11200-011-9034-4).
- Carcione, J. M., S. Picotti, and J. E. Santos, 2012, Numerical experiments of fracture induced velocity and attenuation anisotropy: *Geophysical Journal International*, **191**, 1179–1191, doi: [10.1111/j.1365-246X.2012.05697.x](https://doi.org/10.1111/j.1365-246X.2012.05697.x).
- Carmichael, R. S., 1988, Practical handbook of physical properties of rocks and minerals: CRC Press.
- Castagna, J. P., S. Sun, and R. W. Siegfried, 2003, Instantaneous spectral analysis: Detection of low-frequency shadows associated with hydrocarbons: *The Leading Edge*, **22**, 120–127, doi: [10.1190/1.1559038](https://doi.org/10.1190/1.1559038).
- Chapman, M., 2003, Frequency dependent anisotropy due to mesoscale fractures in the presence of equant porosity: *Geophysical Prospecting*, **51**, 369–379, doi: [10.1046/j.1365-2478.2003.00384.x](https://doi.org/10.1046/j.1365-2478.2003.00384.x).
- Chapman, M., E. Liu, and X.-Y. Li, 2006, The influence of fluid sensitive dispersion and attenuation on AVO analysis: *Geophysical Journal International*, **167**, 89–105, doi: [10.1111/j.1365-246X.2006.02919.x](https://doi.org/10.1111/j.1365-246X.2006.02919.x).
- Chapman, M., S. V. Zatsepin, and S. Crampin, 2002, Derivation of a microstructural poroelastic model: *Geophysical Journal International*, **151**, 427–451, doi: [10.1046/j.1365-246X.2002.01769.x](https://doi.org/10.1046/j.1365-246X.2002.01769.x).
- Chen, H., Y. Ji, and K. A. Innanen, 2018, Estimation of modified fluid factor and dry fracture weaknesses using azimuthal elastic impedance: *Geophysics*, **83**, no. 1, WA73–WA88, doi: [10.1190/geo2017-0075.1](https://doi.org/10.1190/geo2017-0075.1).

- Chen, H., X. Pan, Y. Ji, and G. Zhang, 2017, Bayesian Markov chain Monte Carlo inversion for weak anisotropy parameters and fracture weaknesses using azimuthal elastic impedance: *Geophysical Journal International*, **210**, 801–818, doi: [10.1093/gji/ggx196](https://doi.org/10.1093/gji/ggx196).
- Chen, H., X. Yin, J. Gao, B. Liu, and G. Zhang, 2015, Seismic inversion for underground fractures detection based on effective anisotropy and fluid substitution: *Science China Earth Sciences*, **58**, 805–814, doi: [10.1007/s11430-014-5022-1](https://doi.org/10.1007/s11430-014-5022-1).
- Crampin, S., 1984, Effective anisotropic elastic constants for wave propagation through cracked solids: *Geophysical Journal International*, **76**, 135–145, doi: [10.1111/j.1365-246X.1984.tb05029.x](https://doi.org/10.1111/j.1365-246X.1984.tb05029.x).
- Eastwood, R. L., and J. P. Castagna, 1987, Interpretation of Vp/Vs ratios from sonic logs: *Shear Wave Exploration, Geophysical Development Service*, **1**, 139–153.
- Fu, B., L. Fu, J. Guo, R. J. Galvin, and B. Gurevich, 2020, Semi-analytical solution to the problem of frequency dependent anisotropy of porous media with an aligned set of slit cracks: *International Journal of Engineering Science*, **147**, 103209, doi: [10.1016/j.ijengsci.2019.103209](https://doi.org/10.1016/j.ijengsci.2019.103209).
- Fu, B., J. Guo, L. Fu, S. Glubokovskikh, R. J. Galvin, and B. Gurevich, 2018, Seismic dispersion and attenuation in saturated porous rock with aligned slit cracks: *Journal of Geophysical Research: Solid Earth*, **123**, 6890–6910, doi: [10.1029/2018JB015918](https://doi.org/10.1029/2018JB015918).
- Galvin, R. J., and B. Gurevich, 2009, Effective properties of a poroelastic medium containing a distribution of aligned cracks: *Journal of Geophysical Research*, **114**, B07305, doi: [10.1029/2008JB006032](https://doi.org/10.1029/2008JB006032).
- Goodway, B., 2001, AVO and Lamé constants for rock parameterization and fluid detection: *CSEG Recorder*, **26**, 39–60.
- Guo, J., B. Gurevich, and D. Shuai, 2020, Frequency-dependent P-wave anisotropy due to scattering in rocks with aligned fractures: *Geophysics*, **85**, no. 2, MR97–MR105, doi: [10.1190/geo2019-0353.1](https://doi.org/10.1190/geo2019-0353.1).
- Guo, J., J. G. Rubino, S. Glubokovskikh, and B. Gurevich, 2018a, Dynamic seismic signatures of saturated porous rocks containing two orthogonal sets of fractures: Theory versus numerical simulations: *Geophysical Journal International*, **213**, 1244–1262, doi: [10.1093/gji/ggy040](https://doi.org/10.1093/gji/ggy040).
- Guo, J., D. Shuai, J. Wei, P. Ding, and B. Gurevich, 2018b, P-wave dispersion and attenuation due to scattering by aligned fluid saturated fractures with finite thickness: Theory and experiment: *Geophysical Journal International*, **215**, 2114–2133, doi: [10.1093/gji/ggy406](https://doi.org/10.1093/gji/ggy406).
- Gurevich, B., 2003, Elastic properties of saturated porous rocks with aligned fractures: *Journal of Applied Geophysics*, **54**, 203–218, doi: [10.1016/j.jappgeo.2002.11.002](https://doi.org/10.1016/j.jappgeo.2002.11.002).
- Gurevich, B., M. Brajanovski, R. J. Galvin, T. M. Müller, and J. Toms-Stewart, 2009, P-wave dispersion and attenuation in fractured and porous reservoirs: Poroelasticity approach: *Geophysical Prospecting*, **57**, 225–237, doi: [10.1111/j.1365-2478.2009.00785.x](https://doi.org/10.1111/j.1365-2478.2009.00785.x).
- Hale, D., 2013, Dynamic warping of seismic images: *Geophysics*, **78**, no. 2, S105–S115, doi: [10.1190/geo2012-0327.1](https://doi.org/10.1190/geo2012-0327.1).
- Henneke, E. G., 1972, Reflection-refraction of a stress wave at a plane boundary between anisotropic media: *The Journal of the Acoustical Society of America*, **51**, 210–217, doi: [10.1121/1.1912832](https://doi.org/10.1121/1.1912832).
- Hsu, C. J., and M. Schoenberg, 1993, Elastic waves through a simulated fractured medium: *Geophysics*, **58**, 964–977, doi: [10.1190/1.1443487](https://doi.org/10.1190/1.1443487).
- Huang, G., X. Chen, C. Luo, and Y. Chen, 2021a, Dynamic characterization of reservoirs constrained by time-lapse prestack seismic inversion: *IEEE Transactions on Geoscience and Remote Sensing*, **59**, 5549–5562, doi: [10.1109/TGRS.2020.3019526](https://doi.org/10.1109/TGRS.2020.3019526).
- Huang, G., X. Chen, C. Luo, and Y. Chen, 2021b, Mesoscopic wave-induced fluid flow effect extraction by using frequency-dependent prestack waveform inversion: *IEEE Transactions on Geoscience and Remote Sensing*, **59**, 6510–6524, doi: [10.1109/TGRS.2020.3028032](https://doi.org/10.1109/TGRS.2020.3028032).
- Huang, G., J. Li, X. Chen, and C. Luo, 2017, Frequency-dependent AVO reservoir identification method based on sparse constrained inversion spectral decomposition: *Chinese Journal of Geophysics*, **60**, 3984–3994, doi: [10.6038/cjg20171025](https://doi.org/10.6038/cjg20171025).
- Hudson, J. A., 1981, Wave speeds and attenuation of elastic waves in material containing cracks: *Geophysical Journal International*, **64**, 133–150, doi: [10.1111/j.1365-246X.1981.tb02662.x](https://doi.org/10.1111/j.1365-246X.1981.tb02662.x).
- Hudson, J. A., E. Liu, and S. Crampin, 1996, The mechanical properties of materials with interconnected cracks and pores: *Geophysical Journal International*, **124**, 105–112, doi: [10.1111/j.1365-246X.1996.tb06355.x](https://doi.org/10.1111/j.1365-246X.1996.tb06355.x).
- Hui, Z., X. Yang, Q. Z. Hu, and C. B. Cheng, 2011, Strength test and mechanism of softening of chlorite schist: *Soil Engineering and Foundation*, **25**, 45.
- Humbert, P., and F. Plique, 1972, Propriétés élastiques de carbonates rhomboédriques monocristallins: Calcite, magnésite, dolomite: *Comptes Rendus de l'Académie des Sciences*, **275**, 391–394.
- Jakobsen, M., T. A. Johansen, and C. McCann, 2003, The acoustic signature of fluid flow in complex porous media: *Journal of Applied Geophysics*, **54**, 219–246, doi: [10.1016/j.jappgeo.2002.11.004](https://doi.org/10.1016/j.jappgeo.2002.11.004).
- Keith, C. M., and S. Crampin, 1977, Seismic body waves in anisotropic media: reflection and refraction at a plane interface: *Geophysical Journal International*, **49**, 181–208, doi: [10.1111/j.1365-246X.1977.tb03708.x](https://doi.org/10.1111/j.1365-246X.1977.tb03708.x).
- Kumar, D., Z. Zhao, D. J. Foster, D. Dralus, and M. K. Sen, 2019, Frequency-dependent AVO analysis using the scattering response of a layered reservoir: *Geophysics*, **85**, no. 2, N1–N16, doi: [10.1190/geo2019-0167.1](https://doi.org/10.1190/geo2019-0167.1).
- Li, Y., Z. Guo, and C. Liu, 2024, Characterization of fluid-saturated fractures based on seismic azimuthal anisotropy dispersion inversion method: *IEEE Transactions on Geoscience and Remote Sensing*, **62**, 5918017, doi: [10.1109/TGRS.2024.3407134](https://doi.org/10.1109/TGRS.2024.3407134).
- Liu, H., P. Ding, and X. Li, 2021, Frequency-dependent AVAZ for fractured reservoirs: *Exploration Geophysics*, **52**, 511–524, doi: [10.1080/08123985.2020.1843019](https://doi.org/10.1080/08123985.2020.1843019).
- Luo, C., X. Li, and G. Huang, 2018, Hydrocarbon identification by application of improved sparse constrained inverse spectral decomposition to frequency-dependent AVO inversion: *Journal of Geophysics and Engineering*, **15**, 1446–1459, doi: [10.1088/1742-2140/aab1d6](https://doi.org/10.1088/1742-2140/aab1d6).
- Mavko, G., T. Mukerji, and J. Dvorkin, 2020, *The rock physics handbook*: Cambridge University Press.
- Oh, J. W., and T. Alkhalifah, 2016, The scattering potential of partial derivative wave-fields in 3-D elastic orthorhombic media: an inversion perspective: *Geophysical Journal International*, **206**, 1740–1760, doi: [10.1093/gji/ggw238](https://doi.org/10.1093/gji/ggw238).
- Pan, X., G. Zhang, and X. Yin, 2017, Azimuthally anisotropic elastic impedance inversion for fluid indicator driven by rock physics: *Geophysics*, **82**, no. 6, C211–C227, doi: [10.1190/geo2017-0191.1](https://doi.org/10.1190/geo2017-0191.1).
- Pan, X., G. Zhang, and X. Yin, 2018, Azimuthally pre-stack seismic inversion for orthorhombic anisotropy driven by rock physics: *Science China, Earth Sciences*, **61**, 425–440, doi: [10.1007/s11430-017-9124-6](https://doi.org/10.1007/s11430-017-9124-6).
- Peng, L. L., Z. D. Sun, and Y. Y. Zhang, 2013, Fracture prediction and its fluid identification of complex carbonate reservoir: A case study in Ha7 area, Tarim Basin: 83rd Annual International Meeting, SEG, Expanded Abstracts, 3247–3251, doi: [10.1190/segam2013-1204.1](https://doi.org/10.1190/segam2013-1204.1).
- Pointer, T., E. Liu, and J. A. Hudson, 2000, Seismic wave propagation in cracked porous media: *Geophysical Journal International*, **142**, 199–231, doi: [10.1046/j.1365-246x.2000.00157.x](https://doi.org/10.1046/j.1365-246x.2000.00157.x).
- Rüger, A., 1998, Variation of P-wave reflectivity with offset and azimuth in anisotropic media: *Geophysics*, **63**, 935–947, doi: [10.1190/1.1444405](https://doi.org/10.1190/1.1444405).
- Russell, B. H., D. Gray, and D. P. Hampson, 2011, Linearized AVO and poroelasticity: *Geophysics*, **76**, no. 3, C19–C29, doi: [10.1190/1.3555082](https://doi.org/10.1190/1.3555082).
- Russell, B. H., K. Hedlin, F. J. Hilterman, and L. R. Lines, 2003, Fluid-property discrimination with AVO: A Biot-Gassmann perspective: *Geophysics*, **68**, 29–39, doi: [10.1190/1.1543192](https://doi.org/10.1190/1.1543192).
- Schoenberg, M., and J. Protazio, 1992, 'Zoeppritz' rationalized and generalized to anisotropy: *Journal of Seismic Exploration*, **1**, 125–144.
- Schoenberg, M., and C. M. Sayers, 1995, Seismic anisotropy of fractured rock: *Geophysics*, **60**, 204–211, doi: [10.1190/1.1443748](https://doi.org/10.1190/1.1443748).
- Simmons, G., 1965, Single crystal elastic constants and calculated aggregate properties: Technical report, Southern Methodist University Dallas Texas.
- Simmons, G., and F. Birch, 1963, Elastic constants of pyrite: *Journal of Applied Physics*, **34**, 2736–2738, doi: [10.1063/1.1729801](https://doi.org/10.1063/1.1729801).
- Vanorio, T., M. Prasad, and A. Nur, 2003, Elastic properties of dry clay mineral aggregates, suspensions and sandstones: *Geophysical Journal International*, **155**, 319–326, doi: [10.1046/j.1365-246X.2003.02046.x](https://doi.org/10.1046/j.1365-246X.2003.02046.x).
- Wang, Z., H. Wang, and M. E. Cates, 2001, Effective elastic properties of solid clays: *Geophysics*, **66**, 428–440, doi: [10.1190/1.1444934](https://doi.org/10.1190/1.1444934).
- Wilson, A., M. Chapman, and X. Y. Li, 2009, Frequency-dependent AVO inversion: 79th Annual International Meeting, SEG, Expanded Abstracts, 341–345, doi: [10.1190/1.3255572](https://doi.org/10.1190/1.3255572).
- Wu, X., M. Chapman, and E. Angerer, 2015, Interpretation of phase reversals in seismic reflections from attenuating targets: *Geophysical Journal International*, **200**, 690–697, doi: [10.1093/gji/ggu426](https://doi.org/10.1093/gji/ggu426).
- Zhang, L., J. Ba, and J. M. Carcione, 2021, Wave propagation in infinituple porosity media: *Journal of Geophysical Research: Solid Earth*, **126**, e2020JB021266, doi: [10.1029/2020JB021266](https://doi.org/10.1029/2020JB021266).
- Zhang, L., J. Ba, J. M. Carcione, and C. Wu, 2022, Seismic wave propagation in partially saturated rocks with a fractal distribution of fluid-patch size: *Journal of Geophysical Research: Solid Earth*, **127**, e2021JB023809, doi: [10.1029/2021JB023809](https://doi.org/10.1029/2021JB023809).
- Zhao, L., J. Geng, J. Cheng, D.-H. Han, and T. Guo, 2014, Probabilistic lithofacies prediction from prestack seismic data in a heterogeneous carbonate reservoir: *Geophysics*, **79**, no. 5, M25–M34, doi: [10.1190/geo2013-0406.1](https://doi.org/10.1190/geo2013-0406.1).
- Zhao, L., Q. Yao, D.-H. Han, R. Zhou, J. Geng, and H. Li, 2017, Frequency and angle-dependent poroelastic seismic analysis for highly attenuating reservoirs: *Geophysical Prospecting*, **65**, 1630–1648, doi: [10.1111/1365-2478.12492](https://doi.org/10.1111/1365-2478.12492).
- Zimmer, M. A., 2003, Seismic velocities in unconsolidated sands: Measurements of pressure, sorting, and compaction effects: Ph.D. thesis, Stanford University.

Biographies and photographs of the authors are not available.